Materials Today Bio 31 (2025) 101498

Contents lists available at ScienceDirect

Materials Today Bio

journal homepage: www.journals.elsevier.com/materials-today-bio

Epsilon-polylysine microneedle potentiating MXene-mediated photothermal ablation for combating antibiotic-resistant bacterial infections

Dongyi Xian [a,1], Rui Luo [a,1], Qiaoni Lin [a], Liqing Wang [a,b], Xiaoqian Feng [c], Yuwei Zheng [a], Liming Lin [c], Jiaying Chi [a], Yilang Yan [a], Guilan Quan [a], Tingting Peng [a], Zejun Xu [a,d,*], Chuanbin Wu [a,**], Chao Lu [a,e,***]

[a] State Key Laboratory of Bioactive Molecules and Druggability Assessment, Guangdong Basic Research Center of Excellence for Natural Bioactive Molecules and Discovery of Innovative Drugs, College of Pharmacy, Jinan University, Guangzhou, 511436, China
[b] Department of Pharmaceutical and Pharmacological Sciences, Katholieke Universiteit Leuven, B-3000, Leuven, Belgium
[c] School of Pharmaceutical Sciences, Sun Yat-sen University, Guangzhou, 510006, China
[d] Baiyunshan Pharmaceutical General Factory, Guangzhou Baiyunshan Pharmaceutical Holdings Co., Ltd., Guangzhou, 510515, China
[e] Department of Chemistry, University of South Florida, Tampa, FL, 33620, USA

ARTICLE INFO

Keywords:
Dissolving microneedle
MXene
Antimicrobial peptide
Membrane-disruption effect
Photothermal therapy

ABSTRACT

Antimicrobial peptides show promise in enhancing photothermal therapy, but their application is often limited by the challenge of constructing a delivery system that balances efficacy and safety. Our research demonstrated that the bactericidal efficacy of V_2C MXene-mediated photothermal therapy is enhanced in a concentration-dependent relationship with the introduction and coating of the antimicrobial peptide ε-polylysine (EPL). EPL exhibited a dual role in enhancing bacterial binding and disrupting bacterial membranes, thereby increasing heat transfer efficiency and reducing bacterial resistance to photothermal ablation. The core strategy of this study was to exploit the combined membranolytic-photothermal effect of EPL and V_2C by extensively applying EPL while regulating V_2C nanosheets usage to prevent overheating. This approach aims to achieve potent bactericidal efficacy through photothermal therapy below 60 °C. Consequently, we developed dissolving microneedles incorporated with V_2C nanosheets, where EPL served as the antimicrobial agent and primary matrix, increasing its loading capacity and minimizing the need for inactive excipients. Notably, this microneedle achieved a 99.9 % reduction in the abundance of methicillin-resistant *Staphylococcus aureus* on infected skin after a single application and resulted in a 92-fold reduction in the bacterial load compared to the group treated with commercial Bactroban ointment, with no apparent toxicity to the mice.

1. Introduction

Skin and soft tissue infections (SSTIs) are localized infections that affect the skin, underlying tissues, and sometimes muscles. SSTIs are primarily caused by bacterial invasion through broken skin and mucous membranes [1,2]. These infections pose a significant global health concern, causing a range of community- and hospital-acquired diseases, potentially leading to death if left untreated [3]. A large-scale study using the HealthCore Integrated Research Database revealed an annual SSTI incidence rate of approximately 48.46 cases per 1000 people. Among these, necrotizing SSTIs are particularly severe, with amputation and mortality rates of 12–20 % and 6–33 %, respectively [4,5]. Despite

* Corresponding author. State Key Laboratory of Bioactive Molecules and Druggability Assessment, Guangdong Basic Research Center of Excellence for Natural Bioactive Molecules and Discovery of Innovative Drugs, College of Pharmacy, Jinan University, Guangzhou, 511436, China.
** Corresponding author. State Key Laboratory of Bioactive Molecules and Druggability Assessment, Guangdong Basic Research Center of Excellence for Natural Bioactive Molecules and Discovery of Innovative Drugs, College of Pharmacy, Jinan University, Guangzhou, 511436, China.
*** Corresponding author. State Key Laboratory of Bioactive Molecules and Druggability Assessment, Guangdong Basic Research Center of Excellence for Natural Bioactive Molecules and Discovery of Innovative Drugs, College of Pharmacy, Jinan University, Guangzhou, 511436, China.
E-mail addresses: xuzejun@byszc.com (Z. Xu), chuanbinwu@jnu.edu.cn (C. Wu), chaolu@jnu.edu.cn (C. Lu).
[1] These authors contributed equally to this work.

https://doi.org/10.1016/j.mtbio.2025.101498
Received 6 October 2024; Received in revised form 13 January 2025; Accepted 16 January 2025
Available online 19 January 2025

the reliance on antibiotics for SSTI treatment, the emergence and spread of multidrug-resistant bacteria and the challenges associated with drug delivery to the lesion site have exacerbated the issue of refractory SSTI. This situation highlights the urgent need to develop novel, efficient, and convenient topical antimicrobial agents that can effectively treat skin infections.

Photothermal therapy (PTT) has emerged as a precise, accurate, and rapid antibacterial therapy [6–10]. It employs photothermal agents (PAs) to convert near-infrared (NIR) light energy into heat, which is suitable for treating localized skin infections, as it damages bacterial cell membranes and denatures enzymes, ultimately causing bacterial death [11–13]. One of the advantages of PTT is its reliance on the classical principle of thermal sterilization, which reduces the likelihood of bacterial resistance developing against the treatment. In addition, PTT offers the benefit of precise control over the heating position using lasers and photosensitizers, making PTT more selective in terms of space and time compared to traditional heating sterilization methods [14]. However, conventional PTT systems often lack sufficient interaction to effectively bind bacteria, although PAs are delivered to the site of infection. This limitation hinders the direct transfer of heat from PAs to bacteria, necessitating an indirect heat transfer pathway from PAs to the surrounding environment to reach the bacteria [15]. This pathway is less efficient and can reduce the overall effectiveness of photothermal ablation, highlighting the requirement of higher local temperatures (over 70 °C) for antibacterial purposes, which in turn poses the risk of scalding normal tissues [16]. Therefore, there is a need to develop efficient systems for combating pathogens using photothermal therapy below 60 °C, which selectively targets and ablates pathogens by controlled heating, while minimizing harm to surrounding tissues.

Recent studies have shown that antimicrobial peptides (AMPs) have the potential to potentiate PTT [17–20]. For example, Dong et al. [21] investigated a hybrid nano-antibacterial system, Dap@Au/Ag nanorods, which can enhance the binding and disruption of methicillin-resistant *Staphylococcus aureus* (*MRSA*) cells by modification of the AMP daptomycin and silver ions, thereby increasing the efficiency of bacterial killing via PTT. Xie et al. [22] co-loaded AMP and PA into a microneedle system and successfully constructed an NIR light-responsive microneedle patch. This patch exhibited a controlled release of AMP W379 under NIR light and demonstrated excellent efficacy against *MRSA* wound biofilms *in vivo*. Although these studies have demonstrated the potential of AMPs as effective antimicrobial adjuvants for PTT, the application of these peptides is often limited by their prohibitive cost, toxicity, and low loading capacity, leading to use of lower doses, which may restrict their synergistic potential in enhancing photothermal antibacterial treatments [23,24]. Moreover, the possibility of balancing efficacy and safety by controlling the dose ratio of AMP and PA remains undiscussed.

To optimize the potentiation of AMPs in PTT, this study introduces a novel antimicrobial microneedle system composed of ε-polylysine (EPL) and vanadium carbide (V_2C) MXene nanosheets (Scheme 1). EPL, characterized by its low cost, low toxicity, and high molecular weight, was employed as the primary constituent of the microneedle tip matrix, while V_2C MXene nanosheets were incorporated as the PA because of their superior photothermal conversion efficiency and extensive absorption spectrum [25]. The EPL microneedle, incorporated with V_2C MXene nanosheets, has the following advantages: (i) The application of macromolecular and antibacterial EPL in the fabrication of microneedles can significantly enhance the loading capacity of EPL at the tips, while minimizing the inclusion of inactive excipients and preserving the mechanical properties of the microneedles. (ii) V_2C MXene nanosheets in the microneedle tip are spontaneously coated with a layer of positively charged EPL, which may improve the efficacy of photothermal bacterial ablation by facilitating the electrostatic binding of negatively charged bacteria to the V_2C MXene nanosheets and shortening the heat transfer

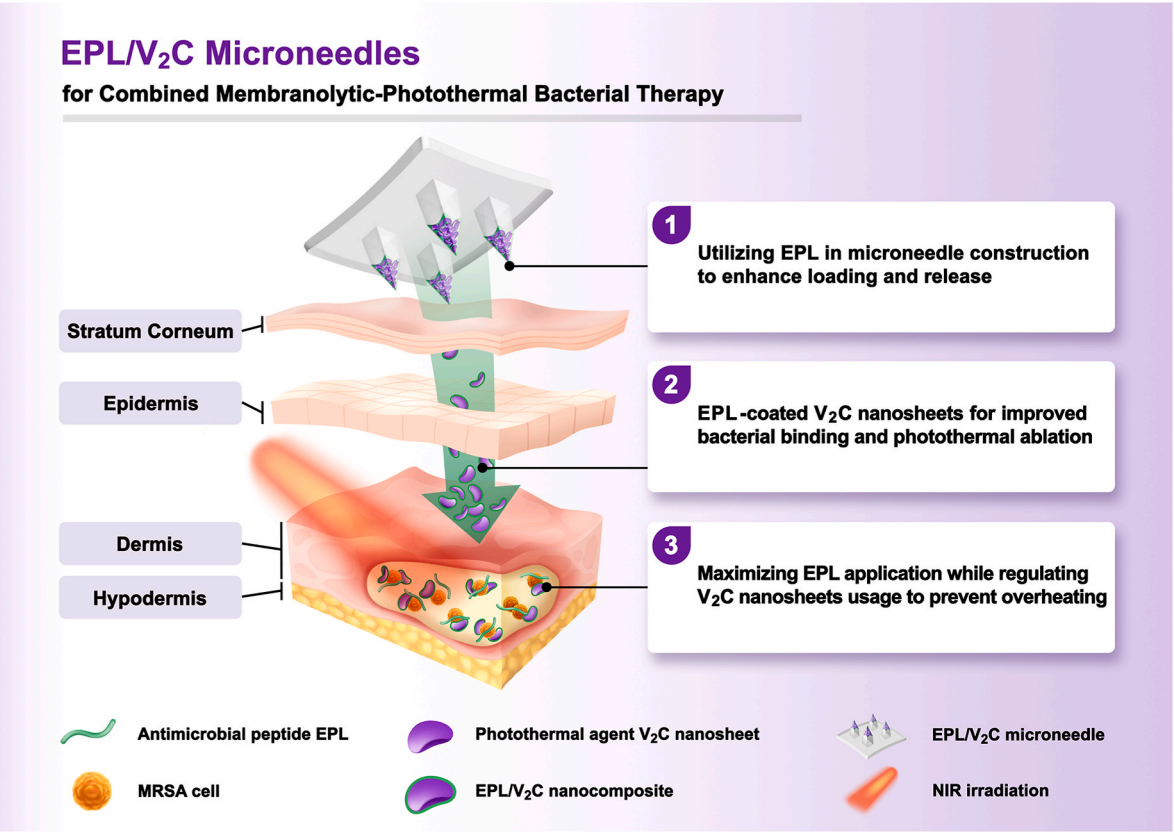

Scheme 1. Dissolving microneedle-mediated transdermal delivery of EPL/V_2C nanocomposites to deep infected site for combating *MRSA* infections by combined membranolytic-photothermal effect.

distance. (iii) Analogous to the shift observed in chemical equilibrium, the combined membranolytic-photothermal effect of the two agents may be significantly enhanced in practical applications through the substantial involvement of EPL, thereby resulting in enhanced efficacy in killing bacteria without the need for excessive local heating.

2. Materials and methods

2.1. Materials and reagents

EPL, with a degree of polymerization ranging from 25 to 35 and a molecular weight of 3.2–4.5 kDa, was supplied by Zhengzhou Bainafo Bioengineering Co., Ltd. (Zhengzhou, China). Polyvinyl alcohol (PVA) with a degree of hydrolysis ranging from 96.8 % to 97.6 % (PVA 103) was obtained from Shanghai Aladdin Biochemical Technology Co., Ltd. (Shanghai, China). Polyvinylpyrrolidone (PVP) with molecular weights of 360.0 kDa (PVP K90) was procured from BASF (Ludwigshafen, Germany). Mueller–Hinton broth and Mueller–Hinton agar (MHA) were purchased from Oxoid Ltd. (Basingstoke, UK). Two percent mupirocin ointment (Bactroban®) was provided by Tianjin Smith Kline & French Laboratories Ltd. (Tianjin, China). *MRSA* (ATCC 33591) and *Pseudomonas aeruginosa* (*P. aeruginosa*, ATCC 27853), *Escherichia coli* (*E. coli*, ATCC 25922), were obtained from the American Type Culture Collection (ATCC, USA) and reconstituted in accordance with the recommended protocols. All commercially available reagents and solvents were utilized as received, without any additional purification.

2.2. Animals

All experimental animal procedures were conducted in strict compliance with the ethical guidelines established by the Experimental Animal Ethics Committee of Jinan University (Approval number: 20230306-0027). Male Sprague–Dawley rats aged 7–8 weeks with body weights of 210 ± 10 g, as well as male Institute of Cancer Research (ICR) mice aged 5–6 weeks with body weights of 20 ± 2 g, were obtained from the Guangdong Medical Laboratory Animal Center. The animals were housed under sterile conditions, with a 12-h light/dark cycle and ad libitum access to food and water.

2.3. Synthesis of V_2C MXene nanosheets

To synthesize the V_2C MXene nanosheets, V_2AlC powder was utilized as the MAX phase precursor. Two grams of V_2AlC powder was dispersed in 40 mL of 48 % hydrofluoric acid (HF) aqueous solution and stirred continuously for 4 d at room temperature. Subsequently, the multilayer V_2C nanosheets were washed with water and ethanol, followed by dispersion in a 25 wt% aqueous solution of tetrapropylammonium hydroxide (TPAOH). The dispersion was stirred for 1 d at room temperature. To ensure the complete removal of TPAOH, the nanosheets were washed again with water and ethanol, and subsequently collected via centrifugation. The collected nanosheets was then dispersed in nitrogen-deaerated water and sonicated to obtain purified, small, and single-layered V_2C nanosheets.

2.4. Fabrication of EPL/V_2C composite nanosheets suspension

The V_2C suspension was stored at 4 °C in an inert gas atmosphere and then centrifuged at 16,000×*g* for 10 min at 4 °C. The resulting pellet was completely dispersed by adding an aqueous medium and subjecting it to sonication. Subsequently, the V_2C solution was added dropwise to the EPL solution with constant sonication for 30 min to yield a suspension of EPL/V_2C nanocomposites.

2.5. Structural characterization of nanosheets

Scanning electron microscopy (SEM) images of various samples were acquired using a field-emission SEM (Gemini 300, Zeiss, Oberkochen, Germany) at an accelerating voltage of 20 kV. To further investigate the internal structure and crystallographic information, high-resolution transmission electron microscopy (TEM) and selected area electron diffraction (SAED) analyses were conducted using a field-emission TEM (JEM 2100F, JEOL, Tokyo, Japan) operating at an accelerating voltage of 200 kV. Three-dimensional images of the V_2C were obtained with an atomic force microscope (AFM; Dimension ICON, Bruker, Karlsruhe, Germany). The Raman spectra of the samples were recorded using a laser microscopic confocal Raman spectrometer (inVia, Renishaw, Gloucestershire, UK). The electronic valence states of the V_2C MXene were analyzed using an X-ray photoelectron spectrometer (XPS; ESCA-lab250, Thermo Fisher, Waltham, MA, USA). Size distribution and zeta potential values of various samples were measured by the Zetasizer Nano ZS90 (Malvern, Worcestershire, UK) at 25 °C. The Tyndall effect maps of suspensions were obtained by irradiating the sample with a laser beam.

2.6. Cell cytotoxicity assay

A standard cell counting kit-8 (CCK-8) assay was used to evaluate the cytotoxic activity on the human embryonic kidney 293T (HEK-293T) cells and human immortalized keratinocytes (HaCaT) [26,27]. The cells were cultured in Roswell Park Memorial Institute (RPMI)-1640 medium, which was supplemented with 200 mM L-glutamine, 10 % fetal bovine serum, and 1 % penicillin/streptomycin under 5 % CO_2 at 37 °C. Subsequently, the cells were seeded into 96-well plates at a density of 1×10^4 cells per well and incubated for 24 h. The cells were washed with phosphate buffered saline (PBS) and then incubated with various concentrations of complete medium containing a mixture of EPL and V_2C, with a ratio of 75:1. After a 24 h incubation period, 100 μL of fresh medium containing 10 μL of CCK-8 solution was added to each well, and the cells were incubated for an additional 2 h. Finally, the optical density of each well was measured using a microplate reader (ELx800, BioTek, VT, USA) at the wavelength of 450 nm. Cell viability was expressed as a percentage relative to the control cells (100 %).

2.7. Photothermal performance of the EPL/V_2C mixture

To assess the photothermal performance, EPL and V_2C were mixed at a ratio of 75:1 to obtain the EPL/V_2C mixture. The resulting suspension, containing 100 μg mL^{-1} of V_2C, was irradiated with an 808 nm NIR laser at a power density of 1 W cm^{-2} for 15 min, followed by natural cooling to room temperature without irradiation. The temperature changes were recorded at different time intervals using a thermal imaging system (TiS75, Fluke, Everett, WA, USA). Calculation of photothermal conversion efficiency was performed following a previously described method [28].

To assess the photothermal performance of EPL/V_2C nanocomposites, aqueous suspensions with varying concentrations of V_2C ranging from 0 to 400 μg mL^{-1} were prepared [29,30]. Each sample was continuously irradiated with an 808 nm NIR laser at a power density of 1 W cm^{-2} for 15 min. The temperature changes were measured and compared them with those of a control group of pure water.

2.8. Determination of minimum inhibitory concentrations (MICs)

Broth microdilution method was employed to evaluate the efficacy of EPL against *MRSA*, *P. aeruginosa*, and *E. coli*. The bacterial cultures were cultivated to the mid-log phase and adjusted to a concentration of 2×10^5 CFU·mL^{-1} in Mueller-Hinton Broth (MHB). Subsequently, EPL solution was twofold serially diluted in PBS across 96-well plates, with concentrations ranging from 0.78 to 200 μg mL^{-1}. Each well was added 50 μL of the bacterial suspension and incubated for 16–18 h at 37 °C. The absorbance at 600 nm was measured using a microplate reader (BioTek Instruments, USA) to determine the MIC as the lowest concentration of

EPL that completely inhibited bacterial growth. MHB with bacteria served as the positive control, while PBS acted as the negative control.

2.9. Combined antimicrobial activity of EPL and V_2C MXene nanosheets

To further evaluate the combined membranolytic-photothermal therapeutic effect of EPL/V_2C, seven groups were established: control, NIR, EPL, V_2C, V_2C + NIR, EPL/V_2C, and EPL/V_2C + NIR. V_2C nanosheet suspensions were prepared at a range of concentrations (0, 200, 400, 600, 800, and 1000 μg mL^{-1}) and mixed with EPL at various concentrations (0, 0.39, 6.25, and 25 μg mL^{-1}) in a 1.5 mL centrifuge tube. Subsequently, 1×10^6 CFU·mL^{-1} of *MRSA* cells in the mid-logarithmic phase were added to each mixture and incubated for 2 h. For the groups with NIR treatment, namely NIR, V_2C + NIR and EPL/V_2C + NIR, the bacterial cells were exposed to an 808 nm laser at a power density of 1 W cm^{-2} for 15 min. An infrared thermal imaging camera (TiS75, Fluke, Everett, WA, USA) was utilized to monitor the temperature changes in the samples during this period. After 2 h of incubation, the bacterial suspensions from each group were subjected to a 10-fold serial dilution. These diluted suspensions were then spread onto MHA plates and incubated at 37 °C overnight to enumerate the live bacteria.

2.10. Antibacterial performance of degradation products from V_2C nanosheets

The V_2C suspension in ultrapure water was exposed to air and shaken at 150 rpm and 37 °C, until it became a completely clear and transparent solution. Subsequently, the sample was diluted to 0–2000 μg mL^{-1}, and 100 μL of the diluted samples were added to 96-well plates. Then, 100 μL of mid-logarithmic phase *MRSA* suspensions (2×10^8 CFU mL^{-1}) were added to each well. The mixture was exposed to illumination from a 30 W white LED light at a distance of approximately 30 cm for 2 h, while the V_xO_y-treated group was kept in the dark and served as the control. To quantify bacterial viability, the bacterial suspensions from each group were serially diluted 10-fold, plated onto MHA plates, and bacterial viability was calculated using the plate colony counting method.

Reactive oxygen species (ROS) levels were determined using an ROS assay kit with the oxidant-sensitive fluorescent dye dichlorodihydrofluorescein diacetate (DCFH-DA; Beyotime, Nantong, China), following the manufacturer's instructions. A 90 min incubation period was conducted with the addition of 10 μL of 200 μM DCFH-DA to the mixture. Subsequently, the fluorescence intensity was measured using a SpectraMax M2 microplate reader at an excitation wavelength of 485 nm and emission peak at 535 nm.

2.11. Hemolysis assessment

Rat erythrocytes were pelleted via centrifugation, rinsed, and resuspended in PBS to yield a 5 % v/v solution. Fifty microliters of this erythrocyte suspension were incubated at 37 °C for 60 min following the addition of an equivalent volume of EPL across a concentration gradient from 31.3 to 2000 μg mL^{-1}. The samples underwent centrifugation at 1000×*g* for 10 min, and 30 μL of the supernatant was then diluted with 100 μL of PBS in a separate 96-well plate. Negative and positive controls were established using erythrocyte suspensions treated with PBS and 2 % Triton X-100, respectively. Hemolysis was quantified by measuring the absorbance at 540 nm in a microplate reader (BioTek Instruments, USA).

2.12. Morphological characteristics of bacteria

SEM was used to assess the morphological effects of various treatments on *MRSA* and *P. aeruginosa*. Initially, the bacteria were cultured, collected, and washed with PBS, followed by incubation with either PBS, EPL, V_2C, or a combination of EPL/V_2C (1:1), for a total of 4 h. During this incubation, the V_2C + NIR and EPL/V_2C + NIR groups were subjected to irradiation with an 808 nm NIR laser at an intensity of 1 W cm^{-2} for 15 min at the 2 h mark, after which incubation was resumed. All the samples were then washed and fixed overnight in 2.5 % glutaraldehyde at 4 °C. The samples were centrifuged, re-washed with PBS, and further fixed with a 1 % osmium acid solution. After three additional rinses with PBS, the samples were dehydrated using a graded ethanol series from 30 % to 100 % followed by substitution with isoamyl acetate. Critical point drying was employed to remove the solvent, and the samples were subsequently coated and imaged using a SEM (SU8010, Hitachi, Tokyo, Japan).

2.13. Detection of bacterial protein leakage

To detect the leakage of bacterial proteins after various treatments, a bicinchoninic acid (BCA) protein assay kit was utilized [31–33]. MRSA suspensions in the mid-logarithmic phase were mixed with different samples at a concentration of 200 μg mL^{-1}. After a 4 h incubation, the V_2C + NIR and EPL/V_2C + NIR groups were exposed to NIR irradiation at 1 W cm^{-2} for 15 min, followed by further incubation. After a total incubation period of 5 h for all samples, bacterial suspensions were sampled and subjected to appropriate dilution. Subsequently, 10 μL of each dilution was spotted onto MHA plates, which were then incubated at 37 °C and imaged.

Additionally, the supernatant from the mixture of MRSA suspensions and various samples was collected by centrifugation at 5000 g. The supernatant was treated with the BCA solution and incubated according to the kit instructions. Protein leakage was then quantified by measuring the absorbance at 562 nm.

2.14. Fabrication and characterization of EPL/V_2C microneedles

Fabrication of V_2C-loaded EPL microneedles (EPL/V_2C microneedles) was initiated by mixing 550 mg·mL^{-1} EPL solution with an equal volume of 550 mg·mL^{-1} PVA 103 solution and incubating in a water bath set at 70 °C for 1 h. After the mixture temperature was reduced to 40 °C, 7.7 mg·mL^{-1} V_2C nanosheet suspension was added dropwise to the EPL and PVA 103 mixture under sonication to achieve an EPL:V_2C ratio of 75:1. Following 30 min of sonication, the V_2C-containing needle-tip solution was then loaded onto a polydimethylsiloxane (PDMS) mold, followed by centrifugation at 3600 g and 0–10 °C for 10 min to remove excess solution. The mold was subsequently centrifuged again at 3600 g for 45 min within a temperature range of 20–30 °C to compact and concentrate the needle-tip solution. Next, a 260 mg mL^{-1} of PVP K90 ethanol solution was introduced into the mold and centrifuged at 3600 g for an additional 45 min at 0–10 °C. The EPL/V_2C microneedles were then placed in a desiccator and dried for 48 h. The same procedure was employed to fabricate EPL microneedles without the V_2C nanosheets.

The morphology of the fabricated microneedles was examined using a digital microscope (BL-SC1600, BELONA, China) and an inverted microscope (Eclipse Ts2, Nikon, Tokyo, Japan). Moreover, SEM images and corresponding energy-dispersive X-ray spectroscopy (EDS) elemental mappings were acquired to further characterize the morphology of the microneedles and analyze the distribution of the elements using a field-emission SEM (Sigma 300, Zeiss, Jena, Germany).

To evaluate the drug-loading capacity of the microneedles, the needle components of the various microneedle arrays were carefully excised using a scalpel blade and subsequently dissolved in deionized water. The encapsulated EPL content within the samples was then quantified using high-performance liquid chromatography (HPLC; 1290, Agilent, Santa Clara, CA, USA). The quantity of V_2C nanosheets present in the samples was determined through acid digestion using a 1:1 mixture of hydrochloric and nitric acid, followed by analysis via inductively coupled plasma-optical emission spectrometry (ICP-OES; 5110 ICP-OES, Agilent, Santa Clara, CA, USA) to calculate the vanadium loading capacity.

To determine the amount of EPL loaded on the V_2C MXene, a specific volume of 550 μg·mL^{-1} EPL solution was mixed with the V_2C suspension at a ratio of 75:1, and the mixture was incubated for 30 min before being centrifuged. The supernatant was then analyzed for EPL content using HPLC, which allowed for the calculation of the actual amount of EPL coated onto the surface of the V_2C nanosheets. Finally, the EPL loading capacity was calculated by determining the ratio of the mass of EPL to the total mass of the EPL/V_2C nanocomposites.

2.15. Ex-vivo skin insertion test of microneedles

The abdominal skin of male Sprague–Dawley rats was excised and prepared by first shaving with an electric trimmer to remove hair. The skin was then treated with a depilatory cream to ensure complete hair removal and then stored at −20 °C. Prior to the experiment, the skin was immersed in a 0.9 % saline solution for 30 min at room temperature to rehydrate it, before being fixed onto a plate. Microneedle patch samples were then manually pressed onto the skin surface. After a 5 min insertion period, the microneedle patch was removed, and the skin was gently washed with saline to remove any residue.

To observe the micropores created by the microneedles, the skin surface at the insertion site was treated with a 0.4 % (w/v) trypan blue aqueous solution for 5 min. The skin was then washed with saline to remove excess dye, and the distinct micropores created by the microneedles were imaged using a digital camera. The skin puncture rate of the microneedles was calculated by determining the ratio of the blue dots observed on the skin to the total number of needle tips present on the microneedle patch.

For the histological examination of the skin, the tissue was fixed in a 4 % paraformaldehyde solution, embedded in paraffin, and then sectioned and stained with hematoxylin and eosin (H&E). The cross-sectional views of the skin were observed under a light microscope (BX53, Olympus, Tokyo, Japan) to assess the microstructural changes induced by the microneedle insertion.

To determine the dissolution rate of microneedle tips, microneedles were inserted into excised hairless Sprague-Dawley rat skin. The microneedles were extracted at predetermined intervals, and the tips were subsequently imaged using a light microscope (BX53, Olympus, Japan).

2.16. In vivo antimicrobial efficacy evaluation

To assess the *in vivo* antimicrobial efficacy of microneedles, a murine model of *MRSA*-induced deep-skin abscess was established. Initially, healthy male ICR mice were anesthetized with an intraperitoneal injection of sodium pentobarbital at a dosage of 70 mg/kg. The dorsal region of the mice was shaved using an electric razor, followed by the application of a depilatory cream to ensure complete hair removal. Subsequently, a subcutaneous injection of a suspension containing 1×10^7 CFU of *MRSA* in 100 μL of sterile PBS solution was administered into the dorsal area of the mice. After a 24 h period, during which obvious signs of skin redness or swelling were observed, the mice were randomly divided into five groups: control group, Bactroban ointment treatment group (Bactroban), EPL microneedle treatment group (EPL MN), EPL/V_2C microneedle group (EPL/V_2C MN), and EPL/V_2C microneedle group with NIR laser irradiation (EPL/V_2C MN + NIR). Uninfected healthy mice served as normal controls. Fifty milligrams of Bactroban ointment or a single patch of various microneedles was applied to the infected sites for 5 min, followed by fixation with medical adhesive tape for 2 h. After careful removal of the microneedles, mice from the EPL/V_2C MN + NIR groups were further exposed to irradiation using an 808 nm NIR laser at an intensity of 1 W cm^{-2} for a duration of 15 min at the site of microneedle administration. Thermal imaging of the mice was conducted using an infrared thermal camera (TiS75; Fluke, Everett, WA, USA).

After 48 h of bacterial infection, all the mice were sacrificed, and the infected skin tissues were imaged and collected. For histological evaluation, the skin samples were first fixed in 4 % paraformaldehyde, followed by paraffin-embedding and sectioning. These sections were stained with hematoxylin and eosin dye (H&E) and subsequently analyzed under light microscopy. For bacterial clearance evaluation, the infected skin tissues were homogenized in 1 mL of PBS and subjected to a 10-fold serial dilution. The bacterial burden in these tissues was assessed by performing colony counts after inoculation onto MHA plates, while viable colonies were enumerated and captured using a digital camera.

2.17. In vivo biosafety evaluation

To evaluate the skin irritation and systemic toxicity of various agents, mice were administered different antibacterial formulations according to a protocol analogous to that employed in the *in vivo* antimicrobial efficacy evaluation study and then euthanized. At 48 h post-treatment, skin was isolated and fixed in a 4 % paraformaldehyde solution. Similarly, major organs, including the heart, liver, spleen, lungs, and kidneys, were harvested 24 h post-treatment for fixation. These tissues were embedded in paraffin, sectioned, and stained with H&E for histological examination.

2.18. Statistical analysis

All quantitative data are presented as mean ± standard deviation. Statistical analyses were conducted using the SPSS software package for Windows (version 17.0, SPSS Inc., Chicago, IL, USA). Comparative analyses among multiple groups were conducted using one-way analysis of variance, followed by least significant difference multiple-range tests. Statistical significance levels are denoted as follows:*$p < 0.05$, **$p < 0.01$, and ***$p < 0.001$.

3. Results and discussion

3.1. Synthesis and characterization of V_2C MXene nanosheets

To obtain nanoscale PAs with high dispersion and appropriate size, ultrathin V_2C MXene nanosheets were synthesized using a two-step exfoliation and intercalation method (Fig. 1a) [34,35]. The process involved the wet-chemical etching of V_2AlC ceramics using a HF solution to selectively remove the interlaced aluminum (Al) layer. Subsequently, the multilayer V_2C MXene nanosheets were delaminated using TPAOH as an intercalant, which effectively reduced the interlayer interactions. The product was then subjected to sonication, ultimately yielding V_2C MXene nanosheets that were either single- or few-layered.

The morphology of the multilayer V_2C was characterized using SEM imaging. Fig. 1b shows that HF etching induced the expansion of typically tightly packed layers of V_2AlC, transforming them into an accordion-like multilayer V_2C structure [36]. This transformation was further supported by TEM micrographs, which consistently displayed the characteristic accordion structure (Fig. 1c).

The structural and morphological characteristics of V_2C MXene nanosheets were comprehensively analyzed using a combination of imaging and spectroscopic techniques [37]. SEM and TEM images of V_2C MXene nanosheets revealed that the nanosheets were uniform and exhibited a typical two-dimensional nanosheet-like morphology with the lateral size of 50–200 nm (Fig. 1d and e). Further structural analysis was performed using SAED, which confirmed the basal-plane hexagonal symmetry of the V_2C MXene nanosheets (Fig. 1f). AFM was used to further investigate the thickness distribution of the as-prepared V_2C MXene nanosheets (Fig. 1g). The images confirm that the nanosheets exhibit a single- or few-layered structure, with thicknesses of approximately 2 nm and 5 nm, respectively. In addition, the chemical composition of the V_2C nanosheets was elucidated using Raman spectroscopy (Fig. 1h). The peak observed at approximately 144 cm^{-1} confirmed the presence of -O terminated groups in V_2C MXene, while the peaks located

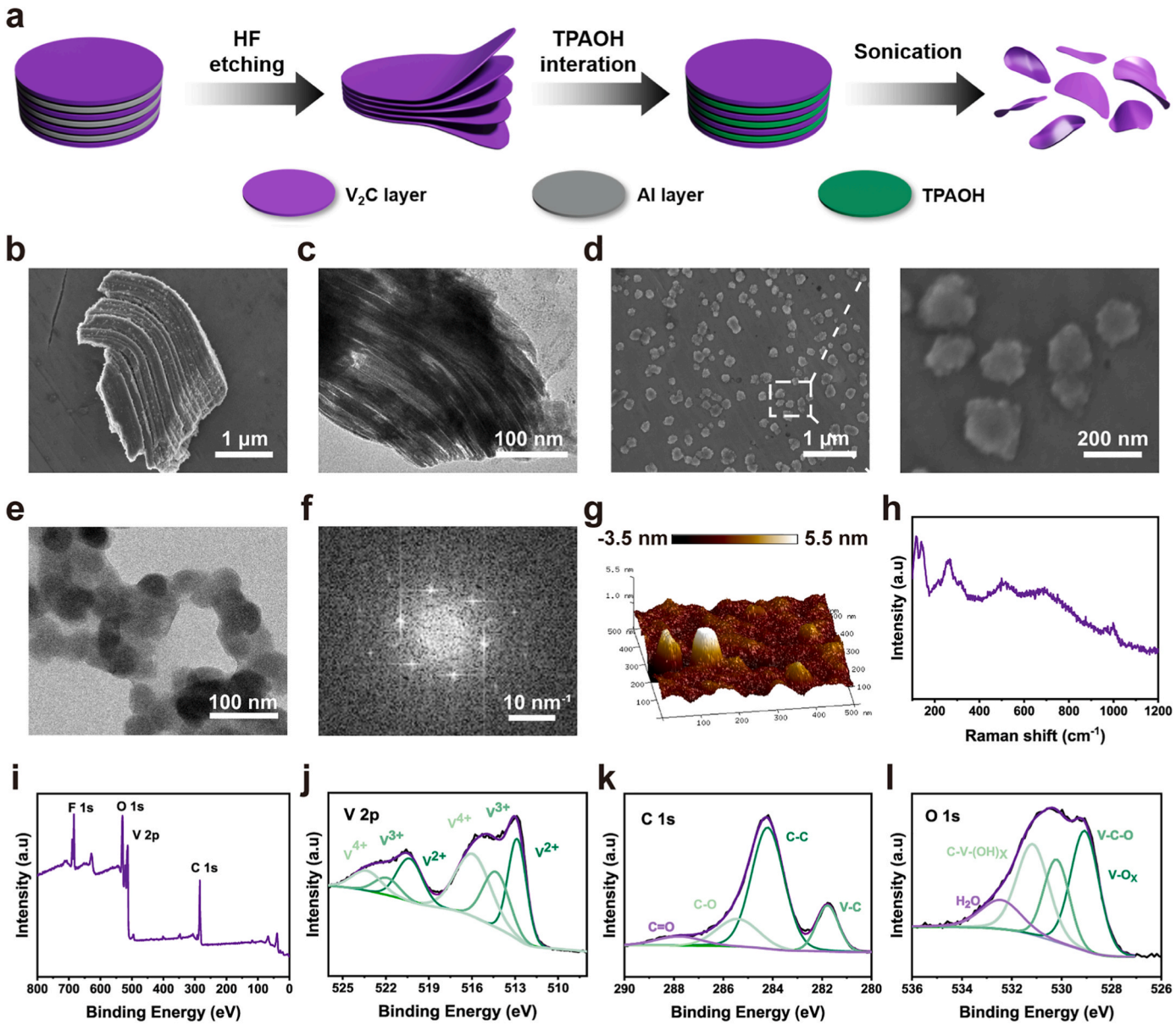

Fig. 1. Synthesis and characterization of V_2C MXene nanosheets and EPL/V_2C nanocomposites. (a) Schematic diagram for the fabrication of V_2C MXene nanosheets. SEM (b) and TEM (c) images of multilayer V_2C. (d) SEM images of single layer V_2C. TEM (e) and SAED (f) image of V_2C MXene nanosheets. (g) AFM image of V_2C nanosheets. (h) Raman spectrum of V_2C MXene nanosheets. XPS spectra for V_2C nanosheets: the survey spectrum (i) and the high-resolution spectra for V 2p (j), C 1s (k), and O 1s (l).

at approximately 219, 267, and 443 cm^{-1} are indicative of the -F and -OH groups on the MXene surface [38].

We further elucidated the chemical composition and oxidation states of the elements present in the V_2C MXene nanosheets through XPS measurement. Fig. 1i presents the survey XPS spectra of the nanosheets, which reveal the prominent peaks of V 2p, C 1s, O 1s, and F 1s across the energy range from 0 to 800 eV. Notably, the absence of significant Al peaks suggests that the Al layer was effectively removed during the etching process. Upon deconvolution of the V 2p region, we identified multiple peaks corresponding to different oxidation states of vanadium: V^{2+} at 512.9 and 520.5 eV, V^{3+} at 514.5 and 522.1 eV, and V^{4+} at 516.1 and 523.4 eV (Fig. 1j). The C 1 s spectrum is decomposed into four peaks, which are attributed to V-C, C-C, C-O, and C=O bonds, located at binding energies of 281.8, 284.2, 285.4, and 287.8 eV, respectively (Fig. 1k). Furthermore, the O 1s is fitted with four contributions at 529.1, 530.2, 531.1, and 532.4 eV, corresponding to V-O_x, V-C-O, C-V-$(OH)_x$, and H_2O, respectively (Fig. 1l). These findings indicate a slight oxidization on the surface of the nanosheets, the presence of oxygen and hydroxyl functional groups, and interlayer water.

3.2. Characterization of EPL/V_2C nanocomposites

It is widely recognized that bacterial cell membranes carry a negative charge. Similarly, V_2C MXene nanosheets also possess a negative charge, which makes it difficult for them to bind to each other due to electrostatic repulsion. However, when these nanosheets are dispersed in a medium containing cationic EPL, they can be spontaneously coated by EPL through electrostatic interactions. This coating potentially leads to the formation of positively charged EPL/V_2C nanocomposites, which are more effective at enhancing bacterial binding.

To investigate the effect of the EPL coating, a series of EPL/V_2C composites were prepared with varying mass ratios of EPL and V_2C. As shown in Fig. 2a, the zeta potential of nanosheets increased from +21.3 to +31.7 mV as the ratio of EPL to V_2C was increased from 1:1 to 75:1.

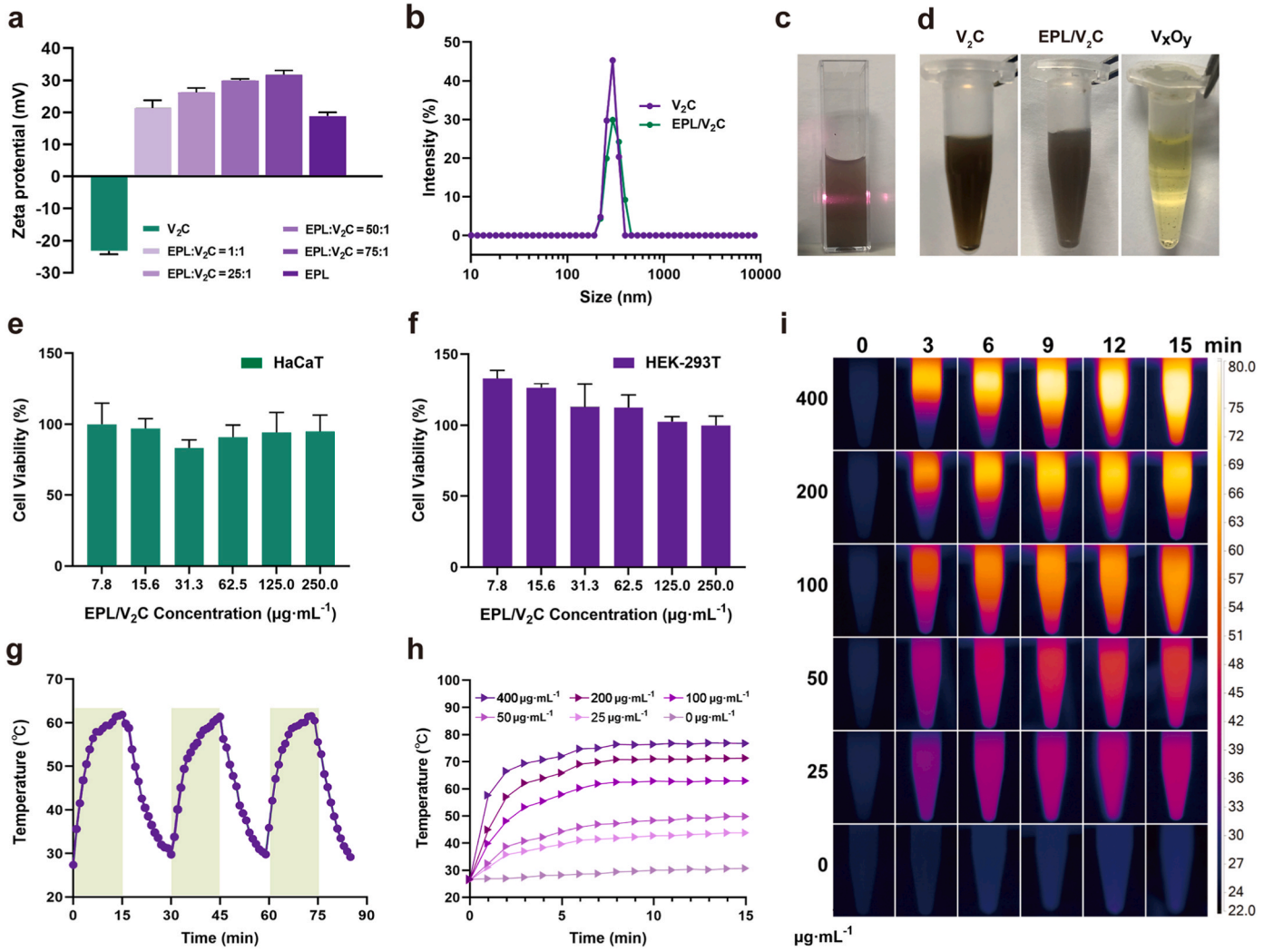

Fig. 2. Characterization of EPL/V_2C nanocomposites. (a) Zeta potentials of V_2C and EPL/V_2C nanocomposites prepared at various mass ratios of EPL to V_2C. (b) Hydrodynamic diameters of V_2C and EPL/V_2C nanocomposites. (c) The Tyndall effect in EPL/V_2C nanocomposite suspension. (d) Digital photographs various samples. Cell viability of HaCaT cells (e) and HEK-293T cells (f) after treatment with different concentrations of EPL/V_2C nanocomposites. (g) Heating curves of an EPL/V_2C nanocomposite suspension containing 100 μg mL^{-1} of V_2C over three laser ON/OFF cycles under a laser (808 nm, 1 W cm^{-2}). Photothermal-heating curves (h) and corresponding thermal images (i) of EPL/V_2C nanocomposite suspension upon laser irradiation (808 nm, 1 W cm^{-2}).

The zeta potential of the composites at elevated EPL ratios surpassed those of uncomplexed EPL. Generally, the higher the absolute value of the zeta potential, the greater the electrostatic repulsion between nanoparticles due to the enhanced double layer effect. According to the DLVO theory, this counteracts van der Waals forces, thus improving colloidal dispersion and preventing aggregation [39]. The experimental findings indicated that the EPL/V_2C composites exhibited enhanced stability in the aqueous phases. This enhanced stability also suggests that V_2C nanosheets in an EPL-rich medium are less likely to aggregate. This characteristic is crucial for maintaining the dispersion of EPL/V_2C composites, particularly during the critical processes of loading and release from the EPL microneedles.

In addition, the EPL/V_2C composites had an aqueous diameter of approximately 200 nm, consistent with the diameter of the V_2C MXene nanosheets (Fig. 2b). Moreover, the presence of the Tyndall effect in the EPL/V_2C composite nanosheet suspension further confirms the homogeneous dispersion of these nanosheets (Fig. 2c). Collectively, these observations indicate that the surface coating provided by EPL did not compromise the dispersibility of the V_2C nanosheets (Fig. 2).

As shown in Fig. 2d, the color of the V_2C nanosheets suspension faded into a transparent yellow solution after being exposed to air for an extended period. This color change indicates the degradability of the nanosheets, which is crucial for their clearance from the body in a physiological environment and ensures minimal long-term impact. To further evaluate the cytocompatibility of the EPL/V_2C composites, HEK-293T and HaCaT cells were selected for cytotoxicity evaluation. These cell lines were chosen for their common use and representative nature, as they are indicative of cells from metabolic organs and the skin, respectively. Fig. 2e and f demonstrated that the EPL/V_2C composites showed low cytotoxicity against both cell types, with cell viability rates exceeding 90 % at a dosage of 250 μg mL^{-1}. The high cytocompatibility of the EPL/V_2C composites suggests that they may possess high selectivity for targeting bacteria over mammalian cells. This selective toxicity is beneficial for the development of nanomedicine intended for antimicrobial applications.

To evaluate the potential of EPL/V_2C composites as PA for PTT, the photothermal performance of V_2C was investigated. The photothermal stability of EPL/V_2C composites were evaluated by laser ON/OFF assays for three cycles (Fig. 2g). Specifically, the temperature fluctuations of EPL/V_2C composites suspension were monitored using an 808 nm NIR laser at a power density of 1 W cm^{-2} for 15 min (laser ON), followed by natural cooling to room temperature for another 15 min (laser OFF). The

maximum temperature of EPL/V_2C composites suspension exhibited no significant deterioration during the three ON/OFF cycles, which strongly indicated their high photothermal stability.

The photothermal heating curves of EPL/V_2C nanocomposite suspension was examined under an 808 nm laser, and both temperature changes and corresponding images were recorded (Fig. 2h and i). Fig. 2h illustrates the temperature elevation of EPL/V_2C nanocomposite suspension at different concentrations of V_2C under 808 nm laser irradiation (1 W cm^{-2}). The temperature rapidly plateaued and rose by approximately 40 °C even at a low concentration of 25 μg mL^{-1} of the sample after 5 min of irradiation. When the V_2C concentration of EPL/V_2C nanocomposite suspension was increased to 400 μg mL^{-1}, the highest temperature recorded was 72 °C after 5 min. The photothermal conversion efficiency of EPL/V_2C composites suspension was calculated to be 21.4 % (Figs. S2 and S3). Consequently, these findings revealed that EPL/V_2C nanocomposites are promising PA candidates for PTT.

3.3. *Combined effect of EPL and V_2C nanosheets on in vitro antibacterial activity*

To confirm the potential of EPL as an antibacterial excipient for microneedles, its antibacterial spectrum was evaluated by determining the MIC of EPL against various pathogens (Fig. 3a). EPL demonstrated broad-spectrum antibacterial activity, with MIC values against *MRSA*, *P. aeruginosa*, and *E. coli* being 12.5, 12.5, and 25 μg mL^{-1}, respectively. To further investigate the impact of heating on EPL during microneedle

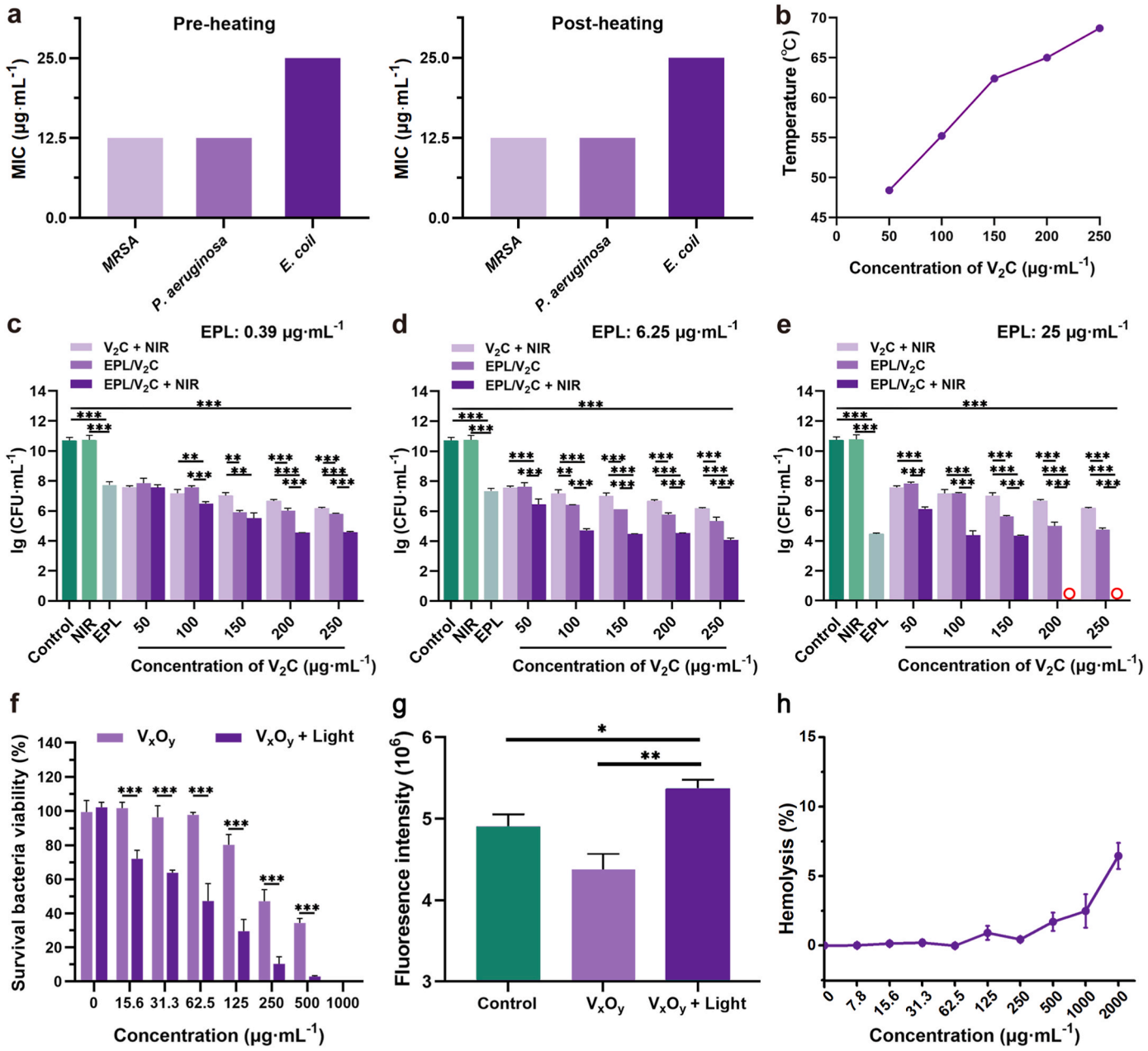

Fig. 3. *In vitro* combined effect of EPL and V_2C nanosheets. (a) MIC values of EPL against various pathogens before and after heating for 30 min. (b) Temperature of EPL-V_2C mixtures after being irradiated with an 808 nm NIR laser at 1 W cm^{-2} for 15 min. Bactericidal efficacy of different concentrations of V_2C nanosheet suspensions when mixed with 0.39 (c), 6.25 (d), and 25 (e) μg·mL^{-1} of EPL solution against MRSA cells. The red circle indicates no viable bacteria were detected. (f) Inhibition of *MRSA* by V_xO_y before and after exposure to visible light. (g) ROS level in *MRSA* after treatment with V_xO_y alone or in combination with visible light exposure. (h) Hemolytic activity of EPL-V_2C mixtures. Significance levels are indicated as $^*p < 0.05$, $^{**}p < 0.01$, and $^{***}p < 0.001$. (For interpretation of the references to color in this figure legend, the reader is referred to the Web version of this article.)

preparation and PTT, EPL was exposed to 60 °C and incubated for 30 min. As shown in Fig. 3a, the heating process had no effect on the MIC value of EPL, which might be due to the fact that its random coil secondary structure did not change because of the heating [40]. Additionally, the inhibitory effect of V_2C nanosheets on MRSA bacteria was evaluated. As shown in Fig. S1, the inhibitory effect of V_2C nanosheets on MRSA increased with increasing concentration, which might be attributed to the fact that V_2C MXene, a two-dimensional material, can exert antibacterial properties through a "nanoknife" mechanism.

To verify the combined effect of EPL on PTT, we prepared a series of mixtures with varying concentrations of EPL solution combined with V_2C nanosheet suspension. The mixtures were subjected to *in vitro* antibacterial activity tests to assess their performance (Fig. 3b–e). Our observations revealed a clear correlation between the concentration of the V_2C nanosheet suspension and the temperature increase. Specifically, when the concentration of the V_2C nanosheet suspension increased from 50 to 250 μg mL^{-1}, the system temperature correspondingly rose to 48, 56, 62.5, 65, and 68 °C (Fig. 3b).

However, even when the concentration of V_2C nanosheets was kept constant to maintain a consistent system temperature, variations in bacterial cell viability were observed, owing to differences in their EPL concentrations within different EPL-V_2C systems. As shown in Fig. S1 and 3c–e, an increase in EPL concentration resulted in a more pronounced photothermal ablation effect for the EPL-V_2C mixture. At a high EPL concentration of 25 μg mL^{-1}, a significant reduction was observed in viable bacterial count within the EPL/V_2C MN + NIR group ($p < 0.001$). These results can be interpreted in conjunction with the previous zeta potential results for different EPL-V_2C mixtures (Fig. 2a). As the V_2C nanosheets were modified by EPL at a high EPL concentration, they carried more positively charged species, which greatly facilitated the transfer of the exothermic heat from the PA to the bacterial cell, owing to their improved binding, thus exerting a better photothermal ablation effect.

Moreover, when V_2C concentration exceeds 200 μg mL^{-1}, all bacteria within the system were found to be completely eradicated. This finding further highlights the potent membranolytic-photothermal effect of the EPL-V_2C combination for bacterial elimination. However, the optimal temperature for PTT in antimicrobial applications should be maintained below 60 °C to prevent damage to surrounding normal tissues. Therefore, adjusting the concentrations of the components within the EPL-V_2C system could be a viable strategy. Increasing the concentration of EPL, rather than that of V_2C nanosheets, could be a more judicious approach. This adjustment is based on the premise that it allows for a controlled increase in the photothermal effect without exceeding the safe temperature threshold. Optimizing the EPL concentration may improve therapeutic safety while preserving the highly effective membranolytic-photothermal combination therapeutic effect of the EPL-V_2C system. This strategy aims to synergistically utilize both AMPs and PAs to ensure their efficacy and safety in the treatment of bacterial infections.

Because V_2C MXene nanosheets are susceptible to oxidative degradation, we explored the antibacterial effects of their degradation products. V_xO_y, which is derived from the natural oxidation of V_2C MXene nanosheets, was mixed with bacteria and exposed to visible light. The results indicated that V_xO_y exhibited concentration-dependent bacterial inhibition, with its antimicrobial activity significantly enhanced under visible-light irradiation (Fig. 3f). To further verify their photocatalytic properties, we measured the ROS levels in V_xO_y treatment cells before and after exposure to visible light. As shown in Fig. 3g, visible-light irradiation induced the production of ROS by V_xO_y. The ROS, with their strong oxidizing potential, are likely to be a key factor in causing bacterial damage, leading to their death. In conclusion, the bacterial inhibition of V_2C MXene nanosheets and the photocatalytic activity of their degradation products further demonstrate the potential long-lasting antibacterial effects of this nanoscale PA in skin infection treatment.

To preliminarily assess the biocompatibility of the EPL-V_2C system, hemolysis assays were performed [41]. As shown in Fig. 3h, the EPL-V_2C mixtures exhibited negligible hemolytic activity, with hemolysis rates remaining below 10 % even at concentrations up to 2000 μg mL^{-1}. Given that the system also demonstrated low cytotoxicity, this indicates a high bactericidal efficacy with minimal side effects, suggesting that the EPL-V_2C system possesses high selectivity and a broad therapeutic window.

3.4. Antibacterial mechanism of EPL/V_2C nanocomposites

To further investigate the mechanism of action of the EPL/V_2C nanocomposites, SEM was employed to examine the morphology and membrane integrity of bacteria after different treatments. SEM images revealed that the *MRSA* bacterial cells in the control group exhibited a regular spherical morphology without any observable defects (Fig. 4a). In contrast, all *MRSA* cells appeared uneven and wrinkled after treatment with various antimicrobial agents. Notably, the combination of EPL and V_2C, particularly with the addition of NIR laser, caused the most severe damage to the cell membrane, as evidenced by the significant leakage of intracellular contents in the EPL/V_2C + NIR group. Similarly, SEM images revealed that *P. aeruginosa* exposed to PBS maintained a rod-shaped and uniform size (Fig. 4b). Conversely, *P. aeruginosa* cells in the EPL, V_2C + NIR, EPL/V_2C, and EPL/V_2C + NIR groups displayed a wrinkled and collapsed state with visible surface damage, particularly in the groups that included EPL.

To further quantify the degree of protein leakage from bacteria following various treatments, a BCA protein assay kit was employed to measure the protein leakage post-treatment. Fig. 4c illustrated that the combination of EPL/V_2C and NIR treatment resulted in the most significant protein leakage ($p < 0.05$), indicating the most obvious bacterial membrane disruption as evidenced by SEM assessments. The obvious membrane disruption is likely the reason for the superior colony inhibition of the EPL/V_2C + NIR group against bacteria compared to other groups (Fig. 4d).

To conclude, these findings demonstrate that V_2C-mediated PTT may cause phospholipids uniformly distributed on the bacterial cell membrane to reach their phase transition temperature, disrupting the original phospholipid bilayer structure and leading to changes in bacterial morphology. Elevated temperatures can denature proteins essential for bacterial homeostasis, promote morphological changes and ultimately lead to bacterial cell death through photothermal ablation mechanisms. The membrane-disruption effects of EPL exacerbates the damage on the bacterial cell membrane [42], which may further weaken their resistance to photothermal ablation. This study elucidates the underlying mechanisms responsible for the significant morphological changes observed in bacteria exposed to EPL/V_2C under NIR laser irradiation, and further substantiates its enhanced antibacterial efficacy *in vitro* antibacterial assays.

3.5. Fabrication of EPL/V_2C microneedles

The dissolution of microneedles offers a promising method for administering therapeutic agents to treat superficial abscess, providing a direct, efficient, and well-dispersed approach for transdermal drug delivery [43–46]. To enhance the antimicrobial potency of V_2C, we explored the possibility of incorporating a high loading of EPL as the primary excipient within the needle tips to maximize the drug-loading capacity while minimizing the use of additional excipients. PVA was selected to enhance the toughness and reduce the brittleness of the EPL microneedles, resulting in improved mechanical properties. Consequently, EPL/V_2C microneedles were fabricated using a mold centrifugal casting method (Fig. 5a). The fabrication process involved PDMS molds derived from a microneedle master through replica molding. This master consisted of an array of 144 (12 × 12) needles with a base width of 300 μm and height of 1200 μm. The needles were designed with a square

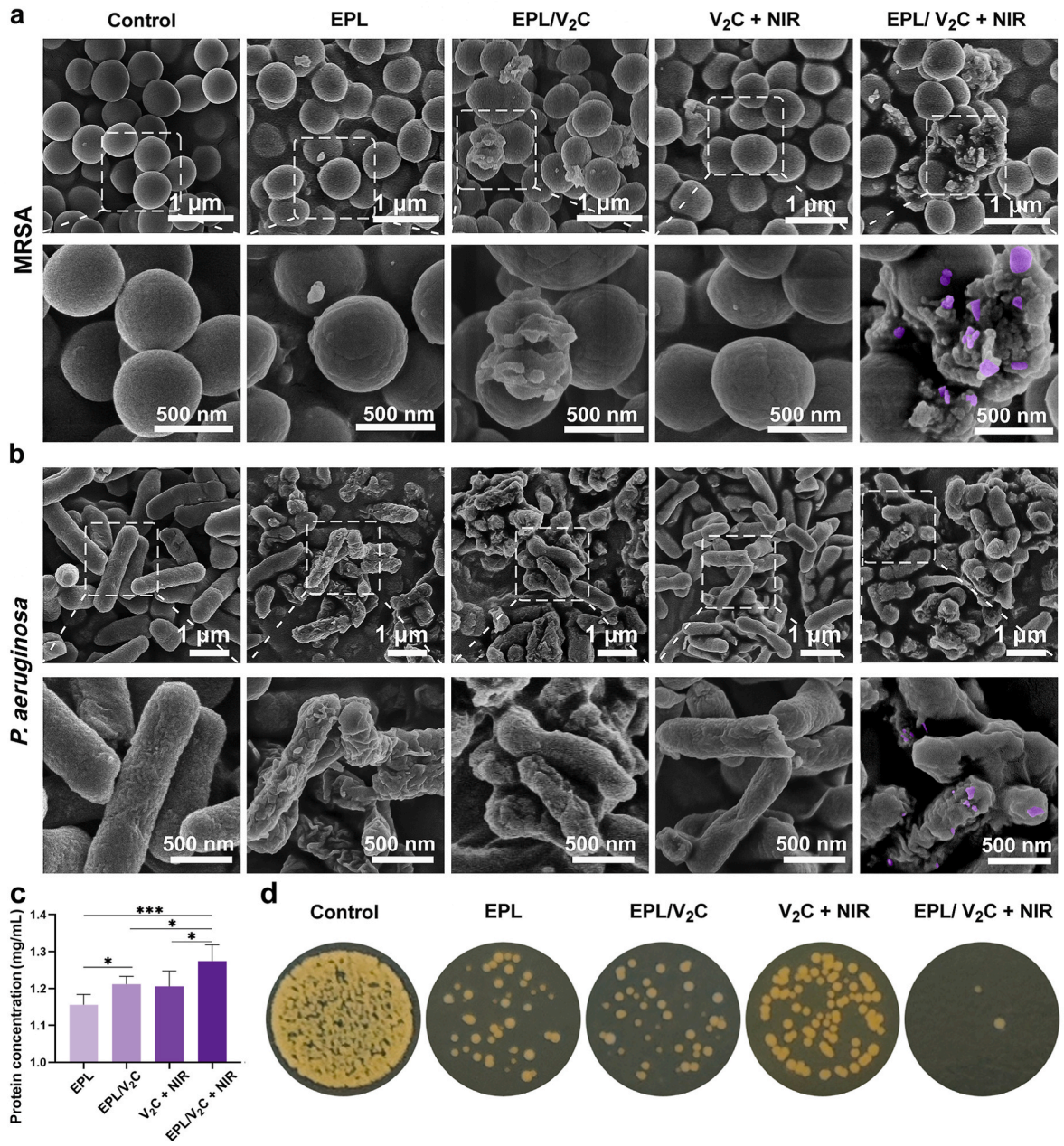

Fig. 4. Antibacterial mechanism of EPL/V_2C nanocomposites. SEM images of MRSA (a) and *P. aeruginosa* (b) after different treatments, where the EPL/V_2C nanocomposites bound to the bacterial cell surfaces in the EPL/V_2C + NIR group are pseudo-coloured purple. Bacterial protein leakage (c) and photographs of *MRSA* bacterial colonies (d) after different treatments. Significance levels are indicated as $^{*}p < 0.05$, and $^{***}p < 0.001$. (For interpretation of the references to color in this figure legend, the reader is referred to the Web version of this article.)

prism base measuring 600 μm and a quadrangular pyramid needle tip with identical dimensions.

As shown in Fig. 5b–e, the fabricated EPL/V_2C microneedle patches exhibited a meticulous and orderly arrangement of individual needles with no evidence of breakage or absence. The black microneedle tips in the digital microscope photograph (Fig. 5b) and the high vanadium signal at the needle tips in SEM-EDS elemental mapping (Fig. 5e) indicate that the EPL/V_2C nanocomposites were concentrated at the tips of the microneedle patches. Moreover, the SEM images verified that the microneedle array structure retained the quadrangular pyramid needle-tip morphology, as originally defined by the molds. The successful preparation of the EPL/V_2C microneedle patches, as evidenced by the morphological characterization, suggests that they have a high potential for efficient skin puncture and stratum corneum barrier breach. By assessing the drug-loading capacity of the microneedles, the encapsulated V_2C content reached 27.1 ± 0.9 μg per patch. Notably, the EPL content reached a remarkable level of 1908.6 ± 4.1 μg per patch, significantly surpassing the majority of commercial topical antimicrobial formulations [47]. This emphasizes the substantial benefits associated with utilizing EPL as the primary matrix material for microneedle fabrication. We further calculated the amount of EPL loaded onto the V_2C MXene, which indicated that the EPL loading capacity was 27.2 %.

To determine the ability of EPL/V_2C to puncture the stratum corneum, we conducted microneedle puncture experiments on rat skin. After microneedle puncture, the rat skin was stained with trypan blue solution, which stains damaged skin tissues. Fig. 5f shows a clear array of micropores demonstrating an average skin puncture efficiency of 96.5 %. Furthermore, H&E staining of rat skin after EPL/V_2C

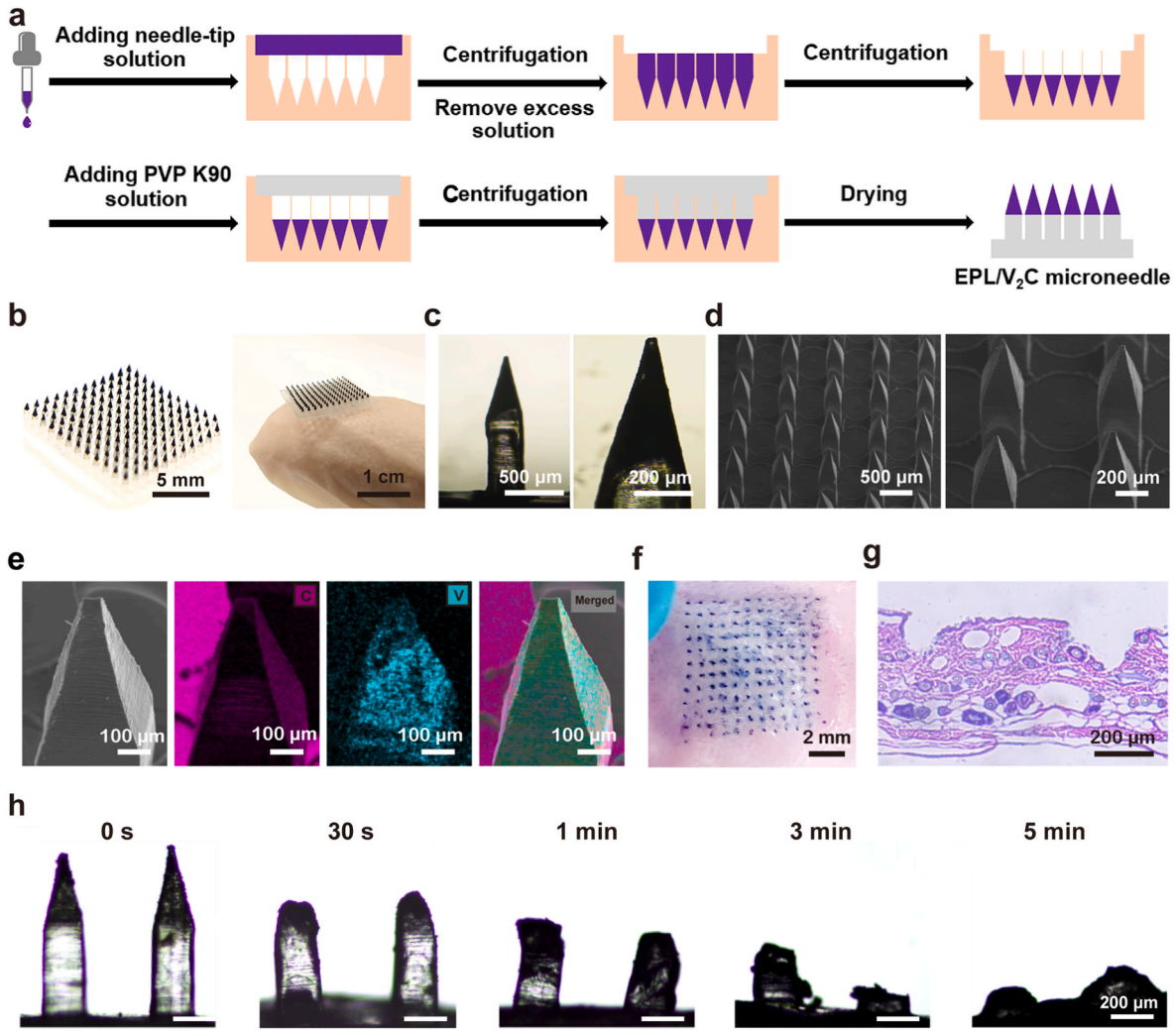

Fig. 5. Fabrication and characterization of the EPL/V_2C microneedles. (a) Schematic illustration of the fabrication process of EPL/V_2C microneedles. Digital camera photos (b) and inverted microscopy images (c) of EPL/V_2C microneedles. SEM images (d) and EDS elemental mapping images (e) of EPL/V_2C microneedles. (f) Photograph of the skin stained with trypan blue after EPL/V_2C microneedles insertion. (g) H&E-stained cross-section of the skin after EPL/V_2C microneedles insertion. (h) Morphology of EPL/V_2C microneedles at different time points after penetrating the skin. (For interpretation of the references to color in this figure legend, the reader is referred to the Web version of this article.)

microneedle administration revealed the successful penetration and formation of well-defined microporous channels with an approximate depth of 350 μm. (Fig. 5g). This finding confirmed the substantial mechanical strength of the EPL/V_2C microneedles, which allows for effective penetration of the stratum corneum (15–20 μm) and epidermis (130–180 μm), thereby facilitating the delivery of EPL/V_2C nanocomposites into the dermal layer (300–2000 μm) [48,49]. These results suggest that the EPL/V_2C microneedles are suitable for the treatment of deep-skin infections.

To assess the dissolution properties of the EPL/V_2C microneedle tips, we conducted experiments to determine their dissolution rate (Fig. 5h). Our results demonstrate that the drug-loaded layer, enriched with EPL and V_2C, dissolves within 1 min of insertion into the skin, while the entire microneedle tip dissolves completely within 5 min. Considering that the primary excipients, EPL and PVA, are established pharmaceutical excipients recognized for their *in vivo* degradation, and V_2C nanosheets have demonstrated the ability to degrade after oxygen exposure, we therefore consider that EPL/V_2C microneedles are biodegradable.

3.6. *In vivo antimicrobial efficacy of EPL/V_2C microneedles against deep-skin infection*

To evaluate the efficacy and convenience of EPL/V_2C microneedles as a topical antimicrobial agent for treating deep-skin infections, we developed a murine model of deep-skin abscess induced by antibiotic-resistant bacteria [50–52]. *MRSA* was chosen as the model pathogen because of its prevalence as the primary cause of SSTI and its significant contribution to mortality associated with antibiotic-resistant bacterial infections globally [53–55]. Subsequently, the therapeutic efficacy of the EPL/V_2C microneedle under NIR laser irradiation was investigated (Fig. 6a). For comparative analysis, the therapeutic effects of Bactroban ointment, EPL microneedles, and EPL/V_2C microneedles without NIR laser irradiation were examined as control treatments (Fig. 6b). Following the administration of EPL/V_2C microneedles, the black EPL/V_2C nanosheets were observed to be released from the microneedle tips and accumulate in the mouse skin tissue, causing a slight black appearance at the infected site. Consequently, while the skin of the model group mice exhibited obvious swelling and inflammatory cell infiltration, the EPL/V_2C MN + NIR treatment group demonstrated the most significant reduction in swelling and abscess shrinkage in the infected skin compared to other treatment groups. The thermographic

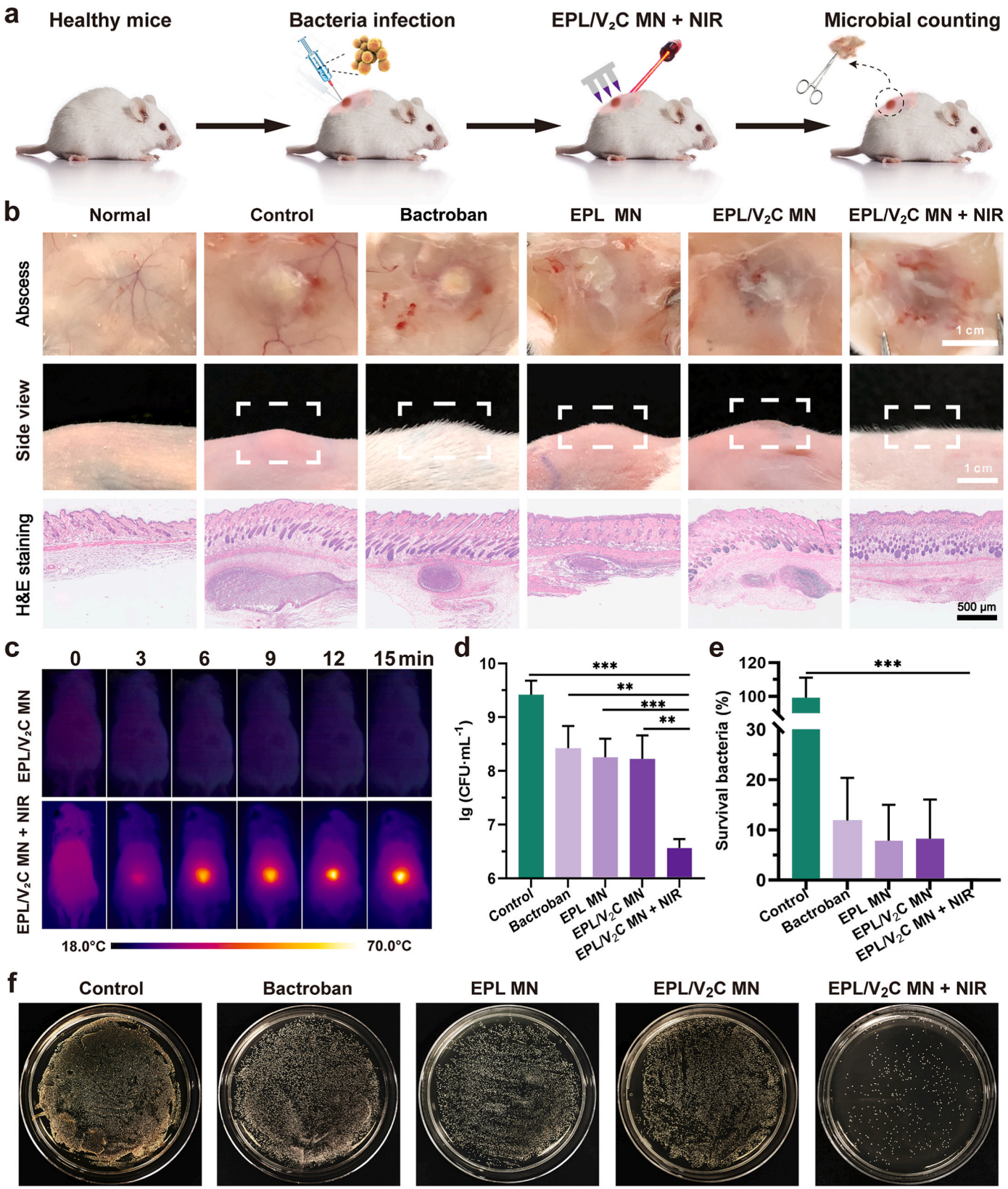

Fig. 6. *In vivo* antimicrobial efficacy of EPL/V_2C microneedles. (a) Schematic of the pharmacodynamics studies on the mouse model of *MRSA*-induced deep-skin infections. (b) Representative images of infected skin and H&E-stained sections depicting the effects of various treatments on infected skin after 48 h of infection. (c) Thermal images of EPL/V_2C microneedles-treated mice under irradiation using an 808 nm laser (1 W cm^{-2}, 15 min). Number of viable *MRSA* bacteria (d) and relative survival rate (e) in the infected skin of mice after different treatments (n = 6). (f) Photographs depicting colonies of *MRSA* on MHA plates obtained by culturing the homogenized sample from infected skin after suitable dilution. Significance levels are indicated as $^{**}p < 0.01$, and $^{***}p < 0.001$.

images presented in Fig. 6c revealed a significant elevation in skin temperature at the *MRSA* infection site following 808 nm NIR laser irradiation after EPL/V_2C microneedle administration. The temperature reached 50 °C in 6 min and was maintained at approximately 58 °C, meeting the antibacterial requirements of PTT while minimizing potential damage to adjacent normal tissues.

To further confirm the effectiveness of the antimicrobial agents, quantitative analyses of the microbial burden in the infected tissues were conducted after 24 h of treatment with different agents (Fig. 6d–f). The antimicrobial effect of EPL microneedles was comparable to that of commercial Bactroban ointment ($p > 0.05$), suggesting that the microneedles with high EPL encapsulation successfully mediated the direct, efficient, and well-dispersed delivery of AMPs near the site of infection. In addition, the number of *MRSA* cells in the EPL/V_2C MN + NIR group was significantly lower than that in the other groups ($p < 0.001$). The EPL/V_2C MN + NIR treatment achieved a high *MRSA* clearance rate of approximately 99.9 %, resulting in a 92- and 61-times lower skin bacterial burden compared to that of the commercial Bactroban ointment and EPL microneedle treatments, respectively.

The significant differences in bacterial burden between the groups indicate the advantage of using an EPL coating to facilitate nanosheet-bacteria binding, shortening the heat transfer distance, and improving the efficacy of photothermal bacterial ablation while reducing heat loss during heat transfer. These results also highlight the high-efficiency *in vivo* therapeutic efficacy of combining membranolytic-photothermal effects, which is substantially enhanced by the involvement of EPL.

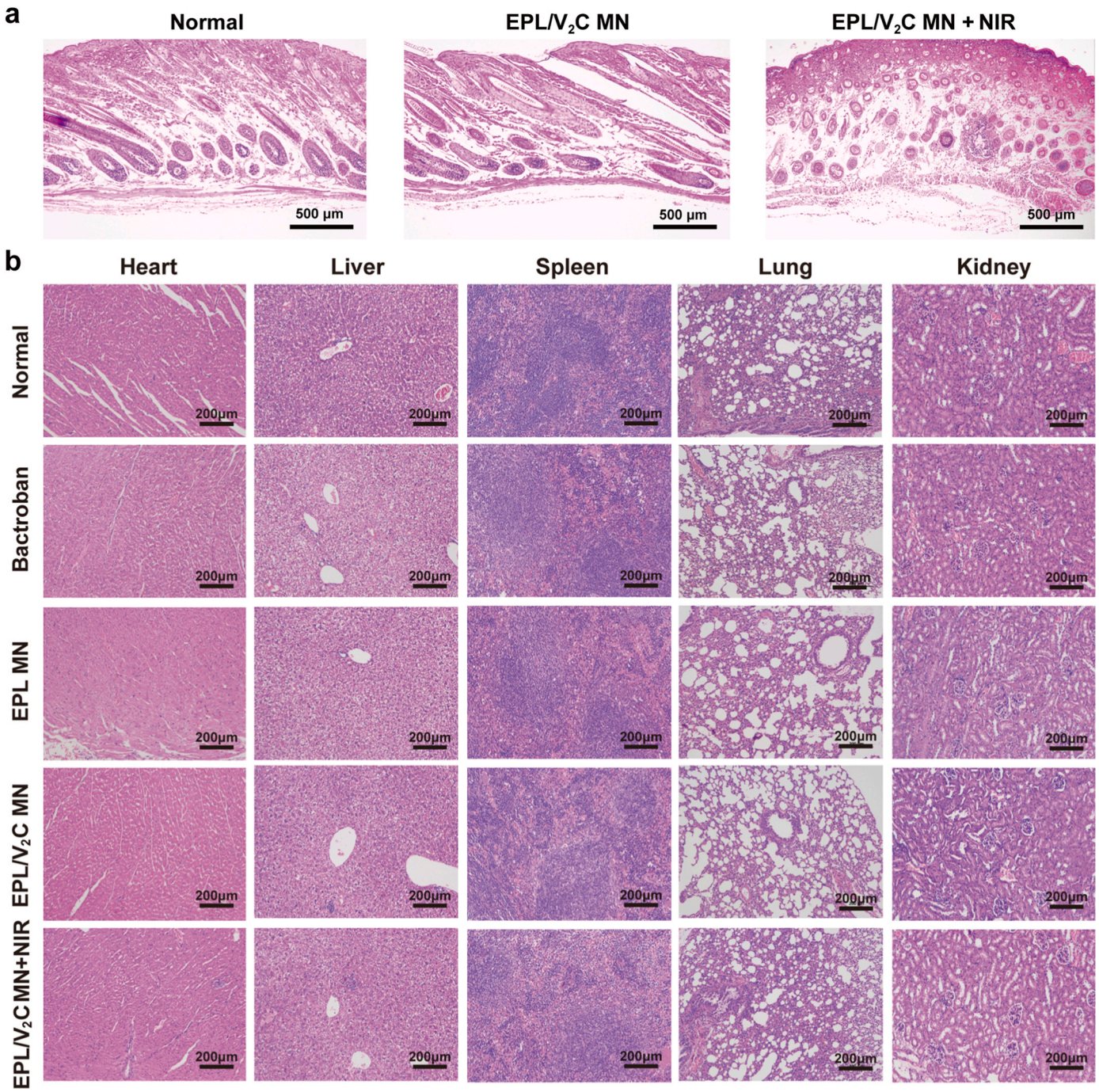

Fig. 7. H&E staining images of skin (a) and major organs (b) of mice after different treatments.

3.7. In vivo toxicology evaluation

It has been reported that drug-loaded microneedles achieve transdermal drug delivery by penetrating the stratum corneum, leading to drug entry into the systemic circulation [47,49]. The liver and kidneys are the major organs involved in drug metabolism and excretion, and nanomedicines delivered via microneedles tend to accumulate significantly in these organs. Therefore, the *in vivo* toxicology evaluation of EPL/V_2C microneedles was performed to assess the risk of skin irritation and the extent of cumulative toxicity by investigating their potential to induce pathological abnormalities in these organs.

To assess the potential for skin irritation associated with EPL/V_2C microneedles therapy, we conducted a comparative analysis of skin histopathology sections following treatment with EPL/V_2C microneedles alone and in combination with NIR. Fig. 7a showed that the skin structure of both groups remained intact, with clear collagen fibers in the dermis, similar to that of healthy mice. This finding suggested that the topical administration of EPL/V_2C microneedles may not cause severe skin irritation.

Additionally, to evaluate the potential cumulative toxicity of EPL/V_2C microneedles on murine organs, we harvested major organ tissues (heart, liver, spleen, lung, and kidneys) from mice for histological analysis after a 24-h treatment with various antibacterial formulations. As shown in Fig. 7b, all treatment groups exhibited good tissue compatibility and low organ toxicity. Notably, the H&E-stained sections of major organ tissues from mice in the EPL/V_2C MN and EPL/V_2C MN + NIR groups exhibited morphological structures consistent with those observed in the normal group. No significant histological abnormalities or pathological changes, including edema, necrosis, or degeneration, were observed. Moreover, the results suggest that the accelerated release and diffusion of antimicrobial agents, potentially induced by NIR laser irradiation during PTT, are unlikely to cause significant toxic side effects.

While V_2O_5 is toxic at high doses, low doses are considered safe and are used in medical treatments. Studies have demonstrated that sequential administration of V_2O_5 at doses below 50 mg/kg over a period of 14 days does not result in lethality in murine models [56]. Our calculations show that the maximum dose of V_2O_5 oxidized from our V_2C-based microneedles is 2.2 mg/kg, which is well below the threshold reported to induce toxicity in mice. This low dose of V_2O_5 administration helps to explain why our V_2C-based microneedles would not cause significant toxicity *in vivo* (Fig. 7). In conclusion, these findings confirm the safety and promising potential of EPL/V_2C microneedles for treating skin infections.

4. Conclusion

In this study, we successfully optimized the antimicrobial performance of V_2C MXene nanosheets by constructing EPL/V_2C microneedles for the transdermal delivery of EPL/V_2C nanocomposites. We experimentally demonstrated that this strategy could induce the spontaneous coating of EPL on the surface of the nanosheets to positively charge the nanoparticles and promote their electrostatic binding with negatively charged bacteria. *In vitro* antibacterial activity studies confirmed that this enhanced bacterial binding greatly reduced the bacterial resistance to EPL/V_2C-mediated photothermal ablation. The binding also significantly enhanced the photothermal sterilization efficiency of EPL/V_2C nanocomposites, and its sterilization efficiency was concentration-dependent with the introduction of EPL. Owing to the high loading of EPL in microneedles (up to 1908.6 ± 4.1 μg per patch), EPL/V_2C microneedles could efficiently kill bacteria at temperatures below 60 °C. In a model of murine deep-skin abscess caused by drug-resistant *MRSA*, EPL/V_2C microneedles demonstrated antimicrobial efficacy far beyond that of commercial Bactroban ointment, while exhibiting high cytocompatibility and histocompatibility. Thus, this study elucidates the methodology for constructing efficient photothermal antimicrobial microneedles that utilize photothermal therapy below 60 °C for high antimicrobial efficacy, while also highlighting the potential of EPL/V_2C microneedles for further applications.

Over the past decade, a wide variety of polymers have been developed to mimic the structural characteristics of AMPs. These polymers comprise a range of structures such as poly(α-amino acids), poly(β-amino acids), poly(2-oxazolines), polymethacrylamides, poly(methacrylates), polymaleimides, polycarbonates, peptidopolysaccharides, and polynorbornenes, among others [57]. They demonstrate broad-spectrum antimicrobial activities and high molecular weights, possessing the properties of both antimicrobial agents and polymer excipients. Potential applications for these AMP-mimetic polymers may include the fabrication of microneedles, enhancement of bacterial binding efficiency, and improvement of the efficacy of photothermal agents, which may inspire the development of advanced antimicrobial systems derived from EPL/V_2C microneedles.

CRediT authorship contribution statement

Dongyi Xian: Writing – original draft, Methodology, Investigation, Formal analysis, Data curation. **Rui Luo:** Writing – original draft, Methodology, Investigation, Formal analysis, Data curation. **Qiaoni Lin:** Investigation, Formal analysis, Data curation. **Liqing Wang:** Investigation, Formal analysis, Data curation. **Xiaoqian Feng:** Methodology, Formal analysis, Data curation. **Yuwei Zheng:** Investigation, Data curation. **Liming Lin:** Investigation, Data curation. **Jiaying Chi:** Formal analysis, Data curation. **Yilang Yan:** Visualization, Data curation. **Guilan Quan:** Methodology, Investigation. **Tingting Peng:** Methodology, Conceptualization. **Zejun Xu:** Validation, Supervision, Project administration, Methodology, Funding acquisition, Conceptualization. **Chuanbin Wu:** Writing – review & editing, Supervision, Resources, Funding acquisition, Conceptualization. **Chao Lu:** Writing – review & editing, Supervision, Resources, Project administration, Methodology, Funding acquisition, Conceptualization.

Declaration of competing interest

The authors declare that they have no known competing financial interests or personal relationships that could have appeared to influence the work reported in this paper.

Acknowledgements

D. X. and R. L. contributed equally to this work. This work was supported by the Basic and Applied Basic Research Foundation of Guangdong Province (No. 2024A1515030104, 2023A1515110441, and 2024A1515011248), the China Postdoctoral Science Foundation (No. 2023M740789), and the National Natural Science Foundation of China (No. 82330112).

Appendix A. Supplementary data

Supplementary data to this article can be found online at https://doi.org/10.1016/j.mtbio.2025.101498.

Data availability

Data will be made available on request.

References

[1] J.M. Leech, M.O. Dhariwala, M.M. Lowe, K. Chu, G.R. Merana, C. Cornuot, A. Weckel, J.M. Ma, E.G. Leitner, J.R. Gonzalez, K.S. Vasquez, B.A. Diep, T. C. Scharschmidt, Toxin-triggered interleukin-1 receptor signaling enables early-life discrimination of pathogenic versus commensal skin bacteria, Cell Host Microbe 26 (6) (2019) 795–809.

[2] J.P. Burnham, J.P. Kirby, M.H. Kollef, Diagnosis and management of skin and soft tissue infections in the intensive care unit: a review, Intensive Care Med. 42 (12) (2016) 1899–1911.
[3] G.E. Thwaites, M. Scarborough, A. Szubert, E. Nsutebu, R. Tilley, J. Greig, S. A. Wyllie, P. Wilson, C. Auckland, J. Cairns, D. Ward, P. Lal, A. Guleri, N. Jenkins, J. Sutton, M. Wiselka, G.R. Armando, C. Graham, P.R. Chadwick, G. Barlow, N. C. Gordon, B. Young, S. Meisner, P. McWhinney, D.A. Price, D. Harvey, D. Nayar, D. Jeyaratnam, T. Planche, J. Minton, F. Hudson, S. Hopkins, J. Williams, M. E. Török, M.J. Llewelyn, J.D. Edgeworth, A.S. Walker, Ukcirg, Adjunctive rifampicin for Staphylococcus aureus bacteraemia (ARREST): a multicentre, randomised, double-blind, placebo-controlled trial, Lancet 391 (10121) (2018) 668–678.
[4] L.G. Miller, D.F. Eisenberg, H.H. Liu, C.L. Chang, Y. Wang, R. Luthra, A. Wallace, C. Fang, J. Singer, J.A. Suaya, Incidence of skin and soft tissue infections in ambulatory and inpatient settings, 2005-2010, BMC Infect. Dis. 15 (1) (2015) 1–8.
[5] P.D. Fey, B. Saïd-Salim, M.E. Rupp, S.H. Hinrichs, D.J. Boxrud, C.C. Davis, B. N. Kreiswirth, P.M. Schlievert, Comparative molecular analysis of community- or hospital-acquired methicillin-resistant Staphylococcus aureus Antimicrob, Agents Chemother. 47 (1) (2003) 196–203.
[6] Z. Geng, Z. Cao, J. Liu, Recent advances in targeted antibacterial therapy basing on nanomaterials, Explorations 3 (1) (2023) 20210117.
[7] X.Y. Ding, Y.R. Yu, C.Y. Yang, D. Wu, Y.J. Zhao, Multifunctional GO hybrid hydrogel scaffolds for wound healing, Research 2022 (2022) 9850743.
[8] Y. Chen, Y.J. Gao, Y. Chen, L. Liu, A.C. Mo, Q. Peng, Nanomaterials-based photothermal therapy and its potentials in antibacterial treatment, J. Contr. Release 10 (328) (2020) 251–262.
[9] Z.Y. Hu, J. Shan, Y.Y. Cui, L. Cheng, X.L. Chen, X.W. Wang, Nanozyme-incorporated microneedles for the treatment of chronic wounds, Adv. Healthcare Mater. 13 (20) (2024) 2400101.
[10] Y. Ma, K. Jiang, H.R. Chen, Q.Q. Shi, H. Liu, X.Y. Zhong, H.S. Qian, X.L. Chen, L. Cheng, X.W. Wang, Liquid exfoliation of V8C7 nanodots as peroxidase-like nanozymes for photothermal-catalytic synergistic antibacterial treatment, Acta Biomater. 149 (2022) 359–372.
[11] S.Y. Hao, H.C. Han, Z.Y. Yang, M.T. Chen, Y.Y. Jiang, G.X. Lu, L. Dong, H.L. Wen, H. Li, J.R. Liu, L.L. Wu, Z. Wang, F.L. Wang, Recent advancements on photothermal conversion and antibacterial applications over MXenes-based materials, Nano-Micro Lett. 14 (1) (2022) 1–36.
[12] G.M. Chen, L. Lin, Z.Y. Mai, Y. Tang, Q.L. Zhang, G. Chen, Z.B. Li, J.S. Zhang, Y. X. Wang, Y.Y. Yang, Z.Q. Yu, Carrier-free photodynamic bioregulators inhibiting lactic acid efflux combined with immune checkpoint blockade for triple-negative breast cancer immunotherapy, ACS Nano 18 (30) (2024) 19875–19889.
[13] B.C. Zhang, L. Lin, J.Z. Mao, W.S. Mo, Z.B. Li, S.T. Wang, Y. Tang, C.H. Cui, Y. F. Wu, Z.Q. Yu, Self-oxygenated co-assembled biomimetic nanoplatform for enhanced photodynamic therapy in hypoxic tumor, Chin. Chem. Lett. 34 (10) (2023) 108518.
[14] J.W. Xu, K. Yao, Z.K. Xu, Nanomaterials with a photothermal effect for antibacterial activities: an overview, Nanoscale 11 (18) (2019) 8680–8691.
[15] Y.W. Zheng, Y.L. Yan, L.M. Lin, Q. He, H.H. Hu, R. Luo, D.Y. Xian, J.Y. Wu, Y. Shi, F.P. Zeng, C.B. Wu, G.L. Quan, C. Lu, Titanium carbide MXene-based hybrid hydrogel for chemo-photothermal combinational treatment of localized bacterial infection, Acta Biomater. 142 (2022) 113–123.
[16] P. Zhao, Y. Zhang, X.A. Chen, C. Xu, J.Z. Guo, M.G. Deng, X.W. Qu, P.S. Huang, Z. J. Feng, J.M. Zhang, Versatile hydrogel dressing with skin adaptiveness and mild photothermal antibacterial activity for methicillin-resistant staphylococcus aureus-infected dynamic wound healing, Adv. Sci. 10 (11) (2023) 2206585.
[17] L.M. Lin, J.Y. Chi, Y.L. Yan, R. Luo, X.Q. Feng, Y.W. Zheng, D.Y. Xian, X. Li, G. L. Quan, D.J. Liu, C.B. Wu, C. Lu, X. Pan, Membrane-disruptive peptides/peptidomimetics-based therapeutics: promising systems to combat bacteria and cancer in the drug-resistant era, Acta Pharm. Sin. B 11 (9) (2021) 2609–2644.
[18] S.L. Bai, J.X. Wang, K.L. Yang, C.L. Zhou, Y.F. Xu, J.F. Song, Y.X. Gu, Z. Chen, M. Wang, C. Shoen, B. Andrade, M. Cynamon, K. Zhou, H. Wang, Q.Y. Cai, E. Oldfield, S.C. Zimmerman, Y.G. Bai, X.X. Feng, A polymeric approach toward resistance-resistant antimicrobial agent with dual-selective mechanisms of action, Sci. Adv. 7 (5) (2021) eabc9917.
[19] Z.Y. Chen, C.L. Zhou, Y.F. Xu, K. Wen, J.F. Song, S.L. Bai, C.X. Wu, W. Huang, Q. Y. Cai, K. Zhou, H. Wang, Y.J. Wang, X.X. Feng, Y.G. Bai, An alternatingly amphiphilic, resistance-resistant antimicrobial oligoguanidine with dual mechanisms of action, Biomaterials 275 (2021) 120858.
[20] Y.X. Qian, S. Deng, Z.H. Cong, H.D. Zhang, Z.Y. Lu, N. Shao, S.A. Bhatti, C. Zhou, J. G. Cheng, S.H. Gellman, R.H. Liu, Secondary amine pendant β-peptide polymers displaying potent antibacterial activity and promising therapeutic potential in treating MRSA-induced wound infections and keratitis, J. Am. Chem. Soc. 144 (4) (2022) 1690–1699.
[21] X.W. Dong, J. Ye, Y. Chen, T. Tanziela, H. Jiang, X.M. Wang, Intelligent peptide-nanorods against drug-resistant bacterial infection and promote wound healing by mild-temperature photothermal therapy, Chem. Eng. J. 432 (15) (2022) 134061.
[22] Y.J. Su, S.M. Andrabi, S.M.S. Shahriar, S.L. Wong, G.S. Wang, J.W. Xie, Triggered release of antimicrobial peptide from microneedle patches for treatment of wound biofilms, J. Contr. Release 356 (2023) 131–141.
[23] M.J. Li, X. Wang, C. Wang, L. Qiu, Y. Xuan, X.L. Lei, P.J. Jiang, H.L. Shi, J.H. Wang, Antimicrobial peptide-loaded gelatinase-responsive photothermal nanogel for the treatment of Staphylococcus aureus-infected wounds, ACS Biomater. Sci. Eng. 8 (8) (2022) 3463–3472.
[24] B. Wang, D.H. Zhao, Y.T. Li, X.P. Zhou, Z.X. Hui, X.L. Lei, L. Qiu, Y. Bai, C. Wang, J. Xia, Y. Xuan, P.J. Jiang, J.H. Wang, Antimicrobial peptide nanoparticle-based microneedle patches for the treatment of bacteria-infected wounds, ACS Appl. Nano Mater. 6 (8) (2023) 6891–6900.
[25] R.X. Zhao, Y.L. Zhu, L.L. Feng, B. Liu, Y.Y. Hu, H.X. Zhu, Z.Y. Zhao, H. Ding, S. L. Gai, P.P. Yang, Architecture of vanadium-based MXene dysregulating tumor redox homeostasis for amplified nanozyme catalytic/photothermal therapy, Adv. Mater. 36 (2) (2024) 13.
[26] Y.X. Zhou, S.L. Luo, B.Y. Niu, B.Y. Wu, J.T. Fu, Y.T. Zhao, V. Singh, C. Lu, G. L. Quan, X. Pan, J.W. Zhang, C.B. Wu, Ultramild one-step encapsulating method as a modular strategy for protecting humidity-susceptible metal-organic frameworks achieving tunable drug release profiles, ACS Biomater. Sci. Eng. 5 (10) (2019) 5180–5188.
[27] J. Liu, W.F. Wu, J.Y. Hu, S.Y. Zhao, Y.Q. Chang, Q.X. Chen, Y.J. Li, J. Tang, Z. M. Zhang, X. Wu, S.M. Jiao, H.C. Xiao, Q. Zhang, J.R. Du, J.F. Zhao, K.H. Ye, M. Y. Huang, J. Xu, H.B. Zhou, J.X. Zheng, P.H. Sun, Novel benzothiazole derivatives target the Gac/Rsm two-component system as antibacterial synergists against Pseudomonas aeruginosa infections, Acta Pharm. Sin. B 14 (11) (2024) 4934–4961.
[28] D.R. Zhang, L.J. Huang, D.W. Sun, H.B. Pu, Q.Y. Wei, Bio-interface engineering of MXene nanosheets with immobilized lysozyme for light enhanced enzymatic inactivation of methicillin-resistant staphylococcus aureus, Chem. Eng. J. 452 (2) (2023) 139078.
[29] L.Y. Zong, H.X. Wu, H. Lin, Y. Chen, A polyoxometalate-functionalized two-dimensional titanium carbide composite MXene for effective cancer theranostics, Nano Res. 11 (8) (2018) 4149–4168.
[30] X.Q. Huang, B.B. Sheng, H.M. Tian, Q.X. Chen, Y.Q. Yang, B. Bui, J. Pi, H.H. Cai, S. Z. Chen, J.L. Zhang, W. Chen, H.B. Zhou, P.H. Sun, Real-time SERS monitoring anticancer drug release along with SERS/MR imaging for pH-sensitive chemo-phototherapy, Acta Pharm. Sin. B 13 (3) (2023) 1303–1317.
[31] Z.Y. Hu, J. Shan, X. Jin, W.J. Sun, L. Cheng, X.L. Chen, X.W. Wang, Nanoarchitectonics of in situ antibiotic-releasing acicular nanozymes for targeting and inducing cuproptosis-like death to eliminate drug-resistant bacteria, ACS Nano 18 (35) (2024) 24327–24349.
[32] W.Q. Wang, Y.Y. Cui, X.L. Wei, Y. Zang, X.L. Chen, L. Cheng, X.W. Wang, CuCo2O4 Nanoflowers with multiple enzyme activities for treating bacterium-infected wounds via cuproptosis-like death, ACS Nano 18 (24) (2024) 15845–15863.
[33] J. Shan, X. Jin, C.Z. Zhang, M.C. Huang, J.H. Xing, Q.R. Li, Y.Y. Cui, Q. Niu, X. L. Chen, X.W. Wang, Metal natural product complex Ru-procyanidins with quadruple enzymatic activity combat infections from drug-resistant bacteria, Acta Pharm. Sin. B 14 (5) (2024) 2298–2316.
[34] Y. Cao, T.T. Wu, K. Zhang, X.D. Meng, W.H. Dai, D.D. Wang, H.F. Dong, X.J. Zhang, Engineered exosome-mediated near-infrared-II region V2C Quantum Dot delivery for nucleus-target low-temperature photothermal therapy, ACS Nano 13 (2) (2019) 1499–1510.
[35] M. Wu, B.X. Wang, Q.K. Hu, L.B. Wang, A.G. Zhou, The synthesis process and thermal stability of V2C MXene, Materials 11 (11) (2018) 2112.
[36] W. Feng, X.G. Han, H. Hu, M.Q. Chang, L. Ding, H.J. Xiang, Y. Chen, Y.H. Li, 2D vanadium carbide MXenzyme to alleviate ROS-mediated inflammatory and neurodegenerative diseases, Nat. Commun. 12 (1) (2021) 2203.
[37] J.W. Deng, D.Y. Xian, X.P. Cai, S.X. Liao, S.Q. Lei, F.Y. Han, Y.D. An, Q. He, G. L. Quan, C.B. Wu, T.T. Peng, C. Lu, H.H. Zhang, Surface-engineered vanadium carbide MXenzyme for anti-inflammation and photoenhanced antitumor therapy of colon diseases, Adv. Funct. Mater. 33 (31) (2023) 2211846.
[38] F.F. Liu, Y.C. Liu, X.D. Zhao, K.Y. Liu, H.Q. Yin, L.Z. Fan, Prelithiated V2C MXene: a high-performance electrode for hybrid magnesium/lithium-ion batteries by ion cointercalation, Small 16 (8) (2020) 1906076.
[39] W.W. Lei, V.N. Mochalin, D. Liu, S. Qin, Y. Gogotsi, Y. Chen, Boron nitride colloidal solutions, ultralight aerogels and freestanding membranes through one-step exfoliation and functionalization, Nat. Commun. 6 (2015) 8849.
[40] R. Luo, D.Y. Xian, F. Li, G.L. Zhou, L. Jiang, J.Y. Wu, L.M. Lin, Y.W. Zheng, G. Y. Liu, Q. Xu, X. Pan, C.B. Wu, T.T. Peng, G.L. Quan, C. Lu, Epsilon-poly-L-lysine microneedle patch loaded with amorphous doxycycline nanoparticles for synergistic treatment of skin infection, Int. J. Biol. Macromol. 266 (2) (2024) 131383.
[41] J.P. Xiao, M.H. Yin, M. Yang, J.H. Ren, C. Liu, J.L. Lian, X.Y. Lu, Y.C. Jiang, Y. C. Yao, J.B. Luo, Lipase and pH-responsive diblock copolymers featuring fluorocarbon and carboxyl betaine for methicillin-resistant staphylococcus aureus infections, J. Contr. Release 369 (2024) 39–52.
[42] D.H. Zhang, C. Shi, Z.H. Cong, Q. Chen, Y.F. Bi, J.Y. Zhang, K.Q. Ma, S.Q. Liu, J. W. Gu, M.Z. Chen, Z.Y. Lu, H.D. Zhang, J.Y. Xie, X.M. Xiao, L.Q. Liu, W.N. Jiang, N. Shao, S. Chen, M. Zhou, X.Y. Shao, Y.D. Dai, M.Q. Li, L.X. Zhang, R.H. Liu, Microbial metabolite inspired β-peptide polymers displaying potent and selective antifungal activity, Adv. Sci. 9 (14) (2022) 2104871.
[43] Y. Zhang, Y. Xu, H. Kong, J. Zhang, H.F. Chan, J. Wang, D. Shao, Y. Tao, M. Li, Microneedle system for tissue engineering and regenerative medicine, Explorations 3 (1) (2023) 20210170.
[44] S. Wang, M.M. Zhao, Y.B. Yan, P. Li, W. Huang, Flexible monitoring, diagnosis, and therapy by microneedles with versatile materials and devices toward multifunction scope, Research 28 (6) (2023) 128.
[45] C.H. Song, X.X. Zhang, M.H. Lu, Y.J. Zhao, Bee sting-inspired inflammation-responsive microneedles for periodontal disease treatment, Research 18 (6) (2023) 119.
[46] D. Yang, M.L. Chen, Y. Sun, C.A. Shi, W.H. Wang, W.C. Zhao, T. Wen, T. Liu, J. T. Fu, C. Lu, C.B. Wu, G.L. Quan, X. Pan, Microneedle-assisted vaccination combined with autophagy regulation for antitumor immunotherapy, J. Contr. Release 357 (2023) 641–654.

[47] T.T. Peng, Y.Y. Chen, W.S. Hu, Y. Huang, M.M. Zhang, C. Lu, X. Pan, C.B. Wu, Microneedles for enhanced topical treatment of skin disorders: applications, challenges, and prospects, Engineering 30 (2023) 170–189.
[48] S.P. Sullivan, D.G. Koutsonanos, M.D. Martin, J.W. Lee, V. Zarnitsyn, S.O. Choi, N. Murthy, R.W. Compans, I. Skountzou, M.R. Prausnitz, Dissolving polymer microneedle patches for influenza vaccination, Nat. Med. 16 (8) (2010) 915–920.
[49] K. van der Maaden, W. Jiskoot, J. Bouwstra, Microneedle technologies for (trans) dermal drug and vaccine delivery, J. Contr. Release 161 (2) (2012) 645–655.
[50] F. Li, L.M. Lin, J.Y. Chi, H. Wang, M.Q. Du, D.S. Feng, L.Q. Wang, R. Luo, H. P. Chen, G.L. Quan, J.F. Cai, X. Pan, C.B. Wu, C. Lu, Guanidinium-rich lipopeptide functionalized bacteria-absorbing sponge as an effective trap-and-kill system for the elimination of focal bacterial infection, Acta Biomater. 148 (2022) 106–118.
[51] J.T. Fu, T. Liu, X.Q. Feng, Y.X. Zhou, M.L. Chen, W.H. Wang, Y.T. Zhao, C. Lu, G. L. Quan, J.F. Cai, X. Pan, C.B. Wu, A perfect pair: stabilized black phosphorous nanosheets engineering with antimicrobial peptides for robust multidrug resistant bacteria eradication, Adv. Healthcare Mater. 11 (10) (2022) 2101846.
[52] J.T. Fu, Y.X. Zhou, T. Liu, W.H. Wang, Y.T. Zhao, Y. Sun, Y.M. Zhang, W.X. Qin, Z. W. Chen, C. Lu, G.L. Quan, C.B. Wu, X. Pan, A triple-enhanced chemodynamic approach based on glucose powered hybrid nanoreactors for effective bacteria killing, Nano Res. 16 (2) (2023) 2682–2694.
[53] D. Jones, E.F.J. Meijer, C. Blatter, S. Liao, E.R. Pereira, E.M. Bouta, K. Jung, S. M. Chin, P.G. Huang, L.L. Munn, B.J. Vakoc, M. Otto, T.P. Padera, Methicillin-resistant Staphylococcus aureus causes sustained collecting lymphatic vessel dysfunction, Sci. Transl. Med. 10 (424) (2018) eaam7964.
[54] G.J. Moran, A. Krishnadasan, W.R. Mower, F.M. Abrahamian, F. LoVecchio, M. T. Steele, R.E. Rothman, D.J. Karras, R. Hoagland, S. Pettibone, D.A. Talan, Effect of cephalexin plus trimethoprim-sulfamethoxazole vs cephalexin alone on clinical cure of uncomplicated cellulitis a randomized clinical trial, JAMA, J. Am. Med. Assoc. 317 (20) (2017) 2088–2096.
[55] C. Youn, C. Pontaza, Y. Wang, D.A. Dikeman, D.P. Joyce, M.P. Alphonse, M.J. Wu, S.J. Nolan, M.A. Anany, M. Ahmadi, J. Young, A. Tocaj, L.A. Garza, H. Wajant, L. S. Miller, N.K. Archer, Neutrophil-intrinsic TNF receptor signaling orchestrates host defense against Staphylococcus aureus, Sci. Adv. 9 (24) (2023) adf8748.
[56] X.Q. Feng, D.Y. Xian, J.T. Fu, R. Luo, W.H. Wang, Y.W. Zheng, Q. He, Z. Ouyang, S. B. Fang, W.C. Zhang, D.J. Liu, S.J. Tang, G.L. Quan, J.F. Cai, C.B. Wu, C. Lu, X. Pan, Four-armed host-defense peptidomimetics-augmented vanadium carbide MXene-based microneedle array for efficient photo-excited bacteria-killing, Chem. Eng. J. 456 (2023) 141121.
[57] R. Luo, H.H. Xu, Q.N. Lin, J.Y. Chi, T.Z. Liu, B.R. Jin, J.Y. Ou, Z.J. Xu, T.T. Peng, G. L. Quan, C. Lu, Emerging trends in dissolving-microneedle technology for antimicrobial skin-infection therapies, Pharmaceutics 16 (9) (2024) 1188.